2015

Numerical Studies of Models of Self-Assembling Systems

Donovan Paul Ruth
Lehigh University

Follow this and additional works at: http://preserve.lehigh.edu/etd

Part of the Physics Commons

Numerical Studies of Models of Self-Assembling Systems

by

Donovan Paul Ruth

A Dissertation
Presented to the Graduate Committee
of Lehigh University
in Candidacy for the Degree of
Doctor of Philosophy
in
Physics

Lehigh University
May 2015

Approved and recommended for acceptance as a dissertation in partial fulfillment of the requirements for the degree of Doctor of Philosophy.

Donovan Paul Ruth

Numerical Studies of Models of Self-Assembling Systems

_____
Date

_____
James D. Gunton, Dissertation Director, Chair

_____
Accepted Date

Committee Members

_____
Jeffrey Rickman

_____
H. Daniel Ou-Yang

_____
Dimitrios Vavylonis

_____
Anand Jagota

Acknowledgements

I would like to thank my advisor, Professor James Gunton for his guidance over the past few years. He has been the source of endless advice, encouragement, and valuable criticism.

Acknowledgements are also due to Professor Jeffrey Rickman for his suggestions and support as well. He has been akin to a co-advisor and has stepped in many times when aid was needed in programming and algorithms.

I am grateful for my committe members Professors Daniel Ou-Yang, Dimitrios Vavylonis, and Anand Jagota for there time, suggestions, and interesting talks aiding in my scientific development.

Thanks also go to all of the friends I have made during my time at Lehigh. They have been a source of support, insight, and interesting conversation.

I am especially thankful to my family for their constant love and support. They have always encouraged my studies and helped push me to attain my goals.

Finally I am eternally gratefull to my fiance and son. They have been so very supportive and enduring during my late nights and of coding and writing.

Contents

List of Tables

List of Figures

Abstract

Self-assembly processes are of great interest in numerous fields. This work attempts to better understand the aggregation of Janus ellipsoids, the parameter space which Janus ellipsoids can be used for encapsulation, and the adsorption of Y-shaped molecules on a two-dimensional lattice. We first employ Canonical Monte Carlo simulations to approximate a "micellization" temperature, cluster distributions, as well as orientation correlation of interacting Janus ellipsoids with an aspect ratio of 0.6 and an interaction range of 0.2σ. The phase diagram of this system was also approximated through a system of B_2 scaling and a phase diagram calculated for a model of Janus spheres with an interaction range of 0.5σ. Seeing a possibility of encapsulation, we explore parameters of temperature, sphere size, inter-particle interaction range and strength and determine the most efficient areas in parameter space for encapsulation of spheres by Janus ellipsoids. The adsorption of a model of Y-shaped particles on a two-dimensional lattice implemented Grand Canonical Monte Carlo simulations, using histogram reweighting and biasing techniques to determine the phase diagram of this system. The critical temperature of this system was also determined through finite-size scaling. We also explore the effects of patterned lattices on the critical temperature of the system.

Chapter 1

Introduction

In recent years the statistical mechanics of non-spherical molecules, such as polypeptide chains, protein molecules, and patchy colloidal particles has garnered considerable attention as their phase behavior and self-assembly has important scientific implications. Self-assembly is the process in which a system of disordered particles thermodynamically equilibrates into systems of higher order without external forces. The self-assembly process is highly dependent on the size, shape, and interactions between the particles. Examples of self-assembling systems include the folding of polypeptide chains into proteins[1, 2], the formation of lipid bilayers[3, 4, 5, 6, 7], and the adsorption of particles onto substrates[8, 9, 10, 11, 12, 13].

There are many potential uses for self-assembling systems at both the nano and mesoscopic scale. One potentially useful area at the nano-scale involves the self-assembly of block copolymers to form bit patterned media(BPM) as a new replacement technology for hard disks[14]. The idea is to use this process of self-assembly to form smaller volume blocks on the disk to be read, making it possible to increase the amount of data stored. Other outlets for similar block copolymers include building 3D transistors[15], thermoplastic elastomers[16], conducting films[17], and light activated aggregates[18, 19].

Another area of interest on the nano-scale is the implementation of DNA in self-assembling materials. For example, DNA double crossover(DX) molecules can be used as two dimensional tiles to form tesselated patterns [20, 21]. The tiles used
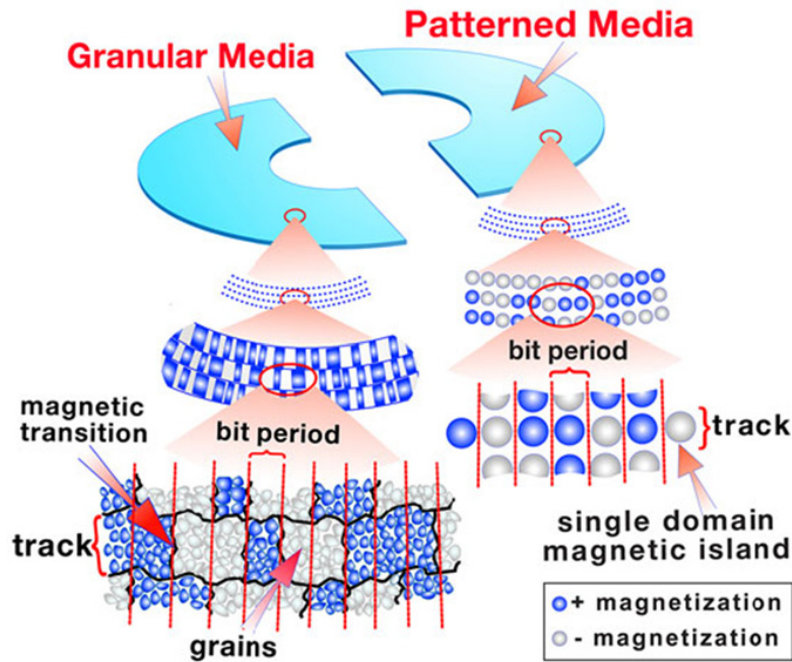
Figure 1.1: "A schematic of how bits are stored in conventional granular media and BPM. Used with permission from HGST."[14]
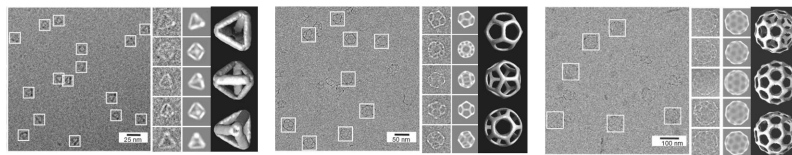
Figure 1.2: From left to right: tetrahedron, dodecahedron, buckyball made from three point DNA motifs[25].

can be of varying size to allow many more complex patterns to arise as well. DNA tensegrity triangles have also been found to be able to form 3D crystals[22], while long single DNA strands can be assembled into polyhedra including octahedra[23] and tetrahedra[24]. Three point motifs were also later used to form tetrahedrons, dodecahedrons, and buckyballs[25].

Among self-assembling systems, there are cases where aggregation is necessary for the proper functioning of cells. For instance aggregation of proteins play key roles

3

in diseases including sickle cell anemia[26], genetic cataracts[27, 28], Alzheimer's disease[29], Parkinson's disease, and Huntington's disease. The formation of cellular compartments is also of great interest. The construction of dense aggregates of proteins and RNA in cells under stress, as well as the assembly and disassembly of cajal bodies over the cell cycle are self-assembly processes. Another self-assembly process during division in germ cells is the formation of germline P granules[30].

One class of self-assembling particles include "patchy" particles. These are particles which can be fabricated to have coatings of varying material, surface coverage, and number of patches. The particles themselves can also be engineered to have numerous shapes including spheres, rods, disks, and polyhedra. Due to the countless possible combinations of particle characteristics, there are vast possible uses for fine-tuned self-assembling systems. Patchy particles can be used to form photonic crystals which allow for the filtering of electromagnetic fields within certain ranges of wavelengths[31], encapsulate guest particles, and as self-healing material among others. Glotzer and Solomon classify the effects of anisotropy by introducing the idea of dimensions of anisotropy which include faceting, patchiness, and aspect ratio[32]. With the massive number of controllable parameters of these self-assembling materials, if one does not know ahead of time which parameters are of interest, much time can be lost by experiment. Some guidance into relevant parameter-space can be determined through computer simulations of model systems.

There are a few advantages to initially studying systems through simulation. The most practical is the time needed for computation versus experiment. Computer simulation of model systems can be of utmost importance in guiding experiment to relevant and interesting results by exploring a wider range of parameters in a shorter amount of time. Many physical characteristics of the model of the self-assembling system can be determined through simulation including pair correlation functions, viscosity, pressure, cluster distributions, and even phase diagrams. The dynamic properties of how these systems self-assemble can also be approximated through simulation.

A very well studied class of patchy particles through both experiment and simulation is that of Janus particles. Janus particles are typically a nano-micrometer

in size, and their surface exhibits two or more distinct physical properties. One of the most well studied cases of Janus particles is the Janus sphere. The spheres typically have two patches, each covering half of the particle, and can have various coating combinations including hydrophobic and hydrophillic[33, 34], opposing charges[35], and metal and non-metal[36]. Many computational studies have been performed on a model of Janus spheres which predict the phase diagram[37, 38], cluster distributions[39], and crystal structures[40].

As stated earlier, one dimension of anisotropy to explore is aspect ratio. Changing the aspect ratio of Janus spheres either by stretching or compressing will form Janus ellipsoids. These types of Janus particles have garnered some attention due to the self-assembly of aggregates[41], formation of fibrils[42], behavior at oil-water interfaces[43, 44], and potential implementation in tissue engineering[45]. Another possible use of these particles is for encapsulation. This is the application which we determined would be of most interest and decided to approach this problem through two studies. The first was to determine the aggregation characteristics of a model of these Janus ellipsoids. The next was to add interactive spheres to determine parameters best suited for encapsulating spheres (e.g. drug particles) with Janus ellipsoids. Some preliminary results of Janus ellipsoid and sphere systems showed promise in oblate ellipsoids with an aspect ratio of 0.6. This led us to study ellipsoids of this type in the beginning section of our work on Janus ellipsoids. In the second section we explore more aspect ratios, among other parameters.

The first part of our simulation study of Janus ellipsoids focuses on estimating the phase diagram, and the characteristics of aggregates formed in the "micelle" gas phase. The phase diagram is essential to aid experimentalists when they wish to replicate certain phases. Our estimates give an approximate boundary of the micelle gas and liquid phase, and also hint at the location of the lamellar phase. We determine the "micellization" temperature, cluster size distribution of the micelle gas at different temperatures and number densities, as well as observe the orientation correlation of interacting particles. All of this combined exposes the temperatures and densities at which aggregates can be found, as well as yields a prediction for the range of cluster sizes found, and structure of the aggregates formed.

5

The second portion of our work on Janus ellipsoids the explores the possibility of encapsulating spheres with Janus ellipsoids. Encapsulation of particles protects them from the local environment, increasing their stability. This process can have many applications in the fields of pharmaceuticals, materials science, and food industries just to name a few. The parameter space examined includes temperature, inter-particle interaction strength and range, and sphere size. We have determined the ideal locations in this parameter space of our model to maximize the number of spheres encapsulated, as well as determined parameters where encapsulation is not favorable.

As mentioned previously, we explored several preliminary studies of the sphere and Janus ellipsoid system prior to the work in the first section. The areas which I studied included a variety of parameters for an interaction range between ellipsoids of 0.5σ. In our studies σ is the characteristic length of the ellipsoid, which is the longest axis end to end. Excluding sphere-sphere interactions and keeping sphere-ellipsoid and ellipsoid-ellipsoid interactions equal, I varied the sphere radius from $0.30 - 3.0\sigma$. Including sphere-sphere interactions which were equivalent to sphere-ellipsoid, I explored a range of sphere radii from $0.30 - 1.5\sigma$. Also explored were ratios of sphere-ellipsoid to sphere-sphere interactions of 1.2 and 1.5, both of which the sphere radius of 0.75σ and 1.0σ. This provided my colleague and collaborator, Dr. Wei Li, with invaluable information in determining which points in parameter space are of greater interest, as well as completing the study as written in Chapter 4. We decided that my focus would be on the study of only short-ranged Janus ellipsoids of aspect ratio equal to 0.6 while he continued our work on encapsulation.

The process of creating these Janus particles in the lab often includes the temporary adsorption of particles onto a substrate in order to be coated with the desired material. Particle adsorption onto a substrate has many potential uses depending on the adsorbent, and the adsorbed molecule. Gas masks implement a form of adsorption to filter air and make it breathable, portable oxygen concentraters use methods of adsorption to increase the amount of Oxygen in air to patients, and certain chromatography techniques rely on adsorption to separate chemicals. Some major areas of interest in materials science and bioengineering include the adsorption of proteins

and polymers onto substrates. Cells interact with other living things through interactions between surface proteins. Biomaterials can encourage cell adsorption and growth if the surface has the correct proteins adsorbed onto the surface[46], whereas polymer surfaces on implants can deter protein adsorption to the surface, therein decreasing interactions with cells, and increase the lifespan of implants as well as decrease the chance of immune or thrombic reactions[47].

The adsorption of organic functional molecules on substrate is also of growing interest. Molecules that motivated this work include C_3 symmetric rigid molecules like trimesic acid, dehydrobenzo[12]annulenes(DBA's), larger tricarboxylic acids, as well as flexible Y-shaped immunoglobulin G. Polymorphism in adlayers of Trimesic acid on graphene can be used to tune electronic properties of the graphene[48], and immunoglobulin G can have many uses both therapeutic and diagnostic due to the specificity with which it binds to antigens. We studied a model of Y-shaped particles on a two dimensional hexagonal lattice to determine the critical temperature, and phase diagram. Substrates can also be patterned by a number of different methods including laser ablating, and many forms of lithography. In future work we will examine how including patterned binding sites effects the critical temperature of the systems.

All of the work presented consists of numerical studies of models of self-assembling systems. To fully understand the methods used, as well as the results ahead, chapter 2 consists of an introduction to the Monte Carlo simulation methods used to determine the physical characteristics of the model systems. The justification for Monte Carlo integration of multi-dimensional integrals is given, along with an explanation of the Metropolis method, detailed balance, and determining acceptance rates of microstate transitions in simulation. All of the aforementioned are the foundation of Monte Carlo simulations. This is the tool used to study model systems in chapters 3-5, and to conduct research in a wide variety of other subjects. The two flavors of Monte Carlo simulations implemented are the Canonical Monte Carlo, and Grand Canonical Monte Carlo simulations. Along with discussing these types, useful tools for Grand Canonical Monte Carlo simulations are discussed including histogram reweighting and biasing to both decrease time of simulation, as well as

to decrease the number of simulations needed to study systems.

In chapter 3 we assess the roles of anisotropy and interaction range on the self-assembly of a model of Janus colloidal particles. In particular, Canonical Monte Carlo simulation is employed to investigate the propensity for the formation of aggregates in a spheroidal model of a colloid having a relatively short-ranged interaction that is consistent with experimentally realizable systems. By monitoring the equilibrium distribution of aggregates as a function of temperature and density, we identify a "micelle" transition temperature and discuss its dependence on particle shape. We find that, unlike systems with longer ranged interactions, this system does not form micelles below a transition temperature at low density. Rather, larger clusters comprising $20 - 40$ particles characterize the transition. We then examine the dependence of the second virial coefficient on particle shape and well width to determine how these important system parameters affect aggregation. Finally, we discuss possible strategies suggested by this work to promote self-assembly for the encapsulation of particles.

In chapter 4 we employ Canonical Monte Carlo simulation to examine the property of encap- sulation in a system comprising Janus oblate spheroids and isotropic spheres. More specifically, the impact of variations in temperature, particle size, inter-particle interaction range and strength are examined for a system in which the spheroids act as the encapsulating agents and the spheres as the encapsulated guests. In this picture, particle interactions are described by a quasi-square-well patch model. This study highlights the environmental adaptation and selectivity of the encapsulation system to changes in temperature and guest particle size, respectively. Moreover, we identify an optimization strategy that promotes encapsulation and an important range in parameter space where sphere encapsulation is favored. Finally, we discuss the generalization of our results to systems having a wide range of particle geometries.

In Chapter 5 we determine the phase diagram of a model of Y-shaped molecules on a hexagonal lattice with and without substrate interactions through Grand Canonical Monte Carlo simulation, using histogram reweighting, multicanonical sampling, and finite-size scaling. We show that (as expected) this model is a member
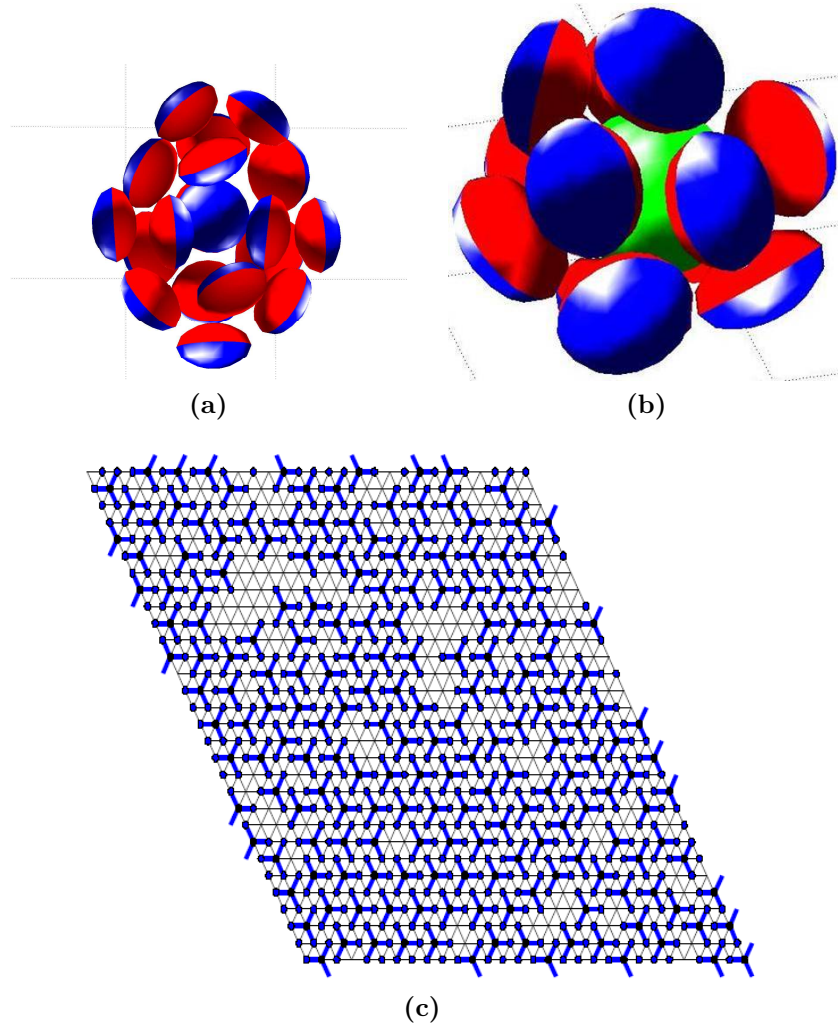
Figure 1.3: a) A cut away of a 30-particle aggregate of Janus ellipsoids. The prevalence of multilayer structures is highlighted here.b) An isotropic sphere encapsulated by Janus ellipsoids. c)Sample of system Y-molecules of system size $L = 30$, at number density $\rho = 0.2156$ and temperature $T = 1.08$.

of the Ising universality class. For low temperatures, we implemented multicanonical sampling to induce faster phase transitions in the simulation. By studying several system sizes, we use finite-size scaling to determine the two phase coexistence curve, including the bulk critical temperature, critical chemical potential, and critical density. We end the thesis with a brief conclusion.

Chapter 2

Monte Carlo Simulation Methods

Monte Carlo methods have been around since the 1940's. While many problems in Physics are deterministic, the calculation of the deterministic quantities can be immensely complex and nearly impossible by typical means. Direct numerical approximation of many dimensional integrals for instance would be costly in terms of computation time, and can have a large margin of error due to the finite sizes of the volumes being added together. Monte Carlo methods are probablistic approaches to approximating deterministic quantities. The purpose of our work in later chapters is to qualitatively estimate characteristics and phase diagrams of simplified models of real systems. Two broad methods of investigating such are molecular dynamics and Monte Carlo simulations. Of the two, all of our work falls under the Monte Carlo category. This is due to the simplicity of implementation, speed of calculations, and vast possible uses. The purpose of this chapter is to introduce Monte Carlo methods executed as the basis of the work done in later chapters.

2.1 Monte Carlo Integration

The purpose of numerical integration is to approximate the value of a definite integral.

$$\int_a^b f(x)\,\mathrm{d}x \tag{2.1}$$

Many methods exist; however a very basic process is followed. That is, the integrand is evaluated at a finite set of points, the points chosen are weighted, and the weighted sum of points are used to approximate the definite integral. The value of a definite integral can be calculated if the average value of the integrand is known over the range $[a, b]$. The integration method of interest is Monte Carlo integration, but first, one needs an idea to start from. Consider the definition of the average value of a continuous function $f(x)$. This is easily identified as

$$\langle f(x) \rangle = \frac{1}{b-a} \int_a^b f(x)\, \mathrm{d}x \tag{2.2}$$

which can be generalized to multiple dimensions as such.

$$\langle f(\overrightarrow{x}) \rangle = \frac{1}{V} \int f(\overrightarrow{x})\, \mathrm{d}\overrightarrow{x} \tag{2.3}$$

$$V = \int \mathrm{d}\overrightarrow{x} \tag{2.4}$$

where $\overrightarrow{x}$ is a multidimensional vector, and V is the total volume of the space being integrated over. If $\langle f(\overrightarrow{x}) \rangle$ can be approximated, then the value of the integral itself can be easily calculated when V is known. Monte Carlo integration attempts to non-deterministically evaluate an integral by approximating the average value of $f(\overrightarrow{x})$ within some error. The simplest way to estimate $\langle f(\overrightarrow{x}) \rangle$ is to randomly select many vectors($\overrightarrow{x_i}$) in the space $\overrightarrow{x}$, evaluate $f(\overrightarrow{x})$ for each selected vector, and then average them. The relation between the randomly selected points $\{\overrightarrow{x_i}\}$, the values of the function at those points $\{f(\overrightarrow{x_i})\}$, and the average value $\langle f(\overrightarrow{x}) \rangle$, is

$$\langle f(\overrightarrow{x}) \rangle = \frac{1}{N} \sum_{i=1}^{N} f(\overrightarrow{x_i}) \tag{2.5}$$

This method will work well assuming that there are no narrow peaks in $f(x)$ as well as each possible $\overrightarrow{x}$ having an equal probability of happening.There are two ways of handling the issue of each $\overrightarrow{x_i}$ having a probability associated with it. The first is to continue choosing in $\overrightarrow{x}$ at random and determine the probabalistic average measurement $\langle f(x) \rangle$ of a probability density function $p(x)$ such that

$$\langle f(x) \rangle = \frac{\sum_{i=1}^{N} f(x_i)p(x_i)}{N \sum_{i=1}^{N} p(x)} \tag{2.6}$$

11

for discrete $p(x)$ and is approximately true for continuous $p(x)$ with large enough N. One disadvantage of this method is that it takes a very large value of N to accurately estimate $\langle f(x) \rangle$, especially if the probability distribution of $\overrightarrow{x}$ has narrow peaks. The second option is to generate $\{\overrightarrow{x_i}\}$ according to their respective relative probabilities. Then, $\langle f(\overrightarrow{x}) \rangle$ could be calculated by

$$\langle f(x) \rangle \approx \frac{1}{N} \sum_{i=1}^{N} n_i f(x_i) \tag{2.7}$$

where n_i is the number of times $f(x_i)$ was generated. The next step is to determine how to generate a large set $\{x_i\}$ according to some probability density function.

2.2 The Metropolis Method

The key part of Eq.2.7 is that one does not need to normalize the probability distribution function in order to be able to generate points. This is ideal for probability distributions which are of great difficulty to normalize, but have relative probability densities which are simply calculated. In statistical mechanics, probability distributions are normalized by the partition function of the system. The partition function is a many dimensional integral with many narrow peaks in $\overrightarrow{x}$ space. For example, the Canonical ensemble is a system with constant N particles, T temperature, and V volume which has a partition function Q defined by

$$Q = c \int \mathrm{d}p^N \mathrm{d}r^N e^{-H(r^N, p^N)/k_B T} \tag{2.8}$$

where p^N is the momenta, and r^N is the position of all N particles in the system, and $H(r^N, p^N)$ is the Hamiltonian of the system which is dependent on all positions and momenta of the particles. The constant k_B is the Boltzmann constant, and c is the proportionality constant which is dependent on the system. Q is analagous to V from the Monte Carlo Integration section. The average measurement of some property A of a system in equilibrium is thus

$$\langle A \rangle = \frac{\int \mathrm{d}p^N \mathrm{d}r^N e^{-H(r^N, p^N)/k_B T}}{Q} \tag{2.9}$$

12

To help simplify things, the dependence of $\langle A \rangle$ on momenta can typically be analytically determined. This is usually easy to do since $H(r^N, p^N) = K + U$ where K is the kinetic energy of the system which is only quadratically dependent on the momenta and U is generally independent of momenta. The average system properties of interest now are only dependent on the average of configurations of the system. We are thus only interested in averages of the form

$$\langle A \rangle = \frac{\int \mathrm{d}r^N e^{-U(r^N)/k_B T}}{Z} \tag{2.10}$$

where Z is the configurational part of the partition function

$$Z = \int \mathrm{d}r^N e^{-U(r^N)/k_B T}. \tag{2.11}$$

It should be noted that the probability density function of a configuration is thus

$$\eta(r^N) = \frac{e^{-\beta U(r^N)}}{Z} \tag{2.12}$$

It is good to point out that any relative probability densities of different configurations are independent of Z, and only dependent on the exponential in the numerator. This characteristic is essential for generating the set of configurations according to the relevant probability distribution. The process of generating the set of configurations involves a random walk in configuration space weighted by the relative probability of going from one configuration to another.

Suppose one has an initial configuration system r_{old}^N, and one wishes to transform the system to the configuration r_{new}^N. The process of the weighted random walk involves starting from an initial configuration, generating a new configuration, calculating the probability of transitioning from the old state to the new state $\nu(old \to new)$, accepting the new configuration based on said probability, and repeat that process until equilibrium is reached and the number of configurations generated is sufficient. Now, the only parts necessary to discuss are determining $\nu(old \to new)$ as well as determining the operation used to take the random walk from r_{old}^N to r_{new}^N.

2.2.1 Detailed Balance

Let us consider generating configurations according to the relevant probability function over an almost infinite number of steps. If the system is in equilibrium, the probability distribution of the configurations generated should be representative of the probable configurations of the system. This also means that the probability of being in a configuration r_{old}^N must not be dependent on the "time" of the system. Here time is used in the sense of the number of iterations the Metropolis scheme has performed. Thus, at any iteration, the probability density of any configuration is independent of the iteration number. One can think of this as the derivative of the probability density function being zero for all iterations.

For an iteration i, and a configuration of interest r_j^N, the change of the probability of being in found in configuration r_j^N would be the probability of entering configuration r_j^N from any configuration possible, minus the probability of being in said configuration and transitioning to any other configuration r_k^N. This can be shown by the equation

$$\sum_k \eta(r_j^N)\nu(j \to k) = \sum_k \eta(r_k^N)\nu(k \to j). \tag{2.13}$$

To simplify the summation over an immense number of states, one can suggest that for each k term

$$\eta(r_j^N)\nu(j \to k) = \eta(r_k^N)\nu(k \to j). \tag{2.14}$$

2.2.2 Acceptance Probability

The transition probability $\nu(j \to k)$ is the product of two probabilities: the probability of generating the new configuration k from the old j, and the probability of accepting that move $a(j \to k)$. The generation of new configurations can be done such that all configurations have an equal probability of being generated; it follows then that

$$\eta(r_j^N)a(j \to k) = \eta(r_k^N)a(j \to k). \tag{2.15}$$

From Eq. 2.15 the ratio of acceptance rates is

$$\frac{a(j \rightarrow k)}{a(k \rightarrow j)} = \frac{\eta(r_k^N)}{\eta(r_j^N)} = e^{-\beta(U(k)-U(j))} \tag{2.16}$$

Once again there are a few choices for choosing the acceptance probability such that this ratio is true, as well as limiting the values of the accpetance probability to be between zero and one. Metropolis *et. al.* chose

$$a(j \rightarrow k) = \begin{cases} e^{-\beta(U(k)-U(j))}, & \text{if } U(k) > U(j) \\ 1, & \text{else} \end{cases} \tag{2.17}$$

A method of altering acceptance rates to encourage rare events will be discussed later in this chapter. For now one has most of the knowledge necessary to generate a large set of configurations based on their relative probability, and average characteristics of systems in equilibrium can be found.

2.3   Canonical Monte Carlo Simulation

The basic algorithm used in Chapter 3 is as follows:

1. Start with a system with particles placed randomly in a simulation box.

2. Choose a particle at random and determine the energy associated with it.

3. Move the particle by a vector $\Delta \vec{r}$ and calculate the energy of the new configuration.

4. Accept the new configuration with the acceptance probability in Eq. 2.17.

5. Rotate the same particle randomly about its center of mass.

6. Accept the new configuration with the acceptance probability in Eq. 2.17.

7. Repeat steps 2-6 many times.

After enough iterations, the configurations generated will be representative of the system in equilibrium and averages can be calculated. Some of these averages include energy, specific heat, cluster distributions, pressure, and structure factor among others.

While dynamic properties of the system can not be studied easily with Monte Carlo methods, there are advantages compared to implementing a molecular dynamics simulation. For instance, there are systems that one would wish to simulate which can take an immensely long time to equilibrate. The typical time scale for molecular dynamics is on the order of a few microseconds, which can take many hours to simulate. MC methods on the other hand do not follow phase space trajectories of these systems and can more easily jump to states closer to equilibrium, decreasing the simulation time. Another advantage to MC comes from the relative order of calculations required. For systems with N particles, the number of calculations for each step is on the order of N, whereas molecular dynamics requires calculations on the order of N^2.

Canonical Monte Carlo (CMC) simulations are good to determine many properties compared to molecular dynamics, but determining phase diagrams for models of systems is rather difficult. To find two phase coexistence in this simulation method would require determining sections of different phases in the volume V as well as the system requiring energy to construct the phase boundaries. The Grand Canonical ensemble can overcome the need for phase boundaries as well as make it easier to determine the different phases.

2.4 Grand Canonical Monte Carlo Simulation

This type of simulation has constant temperature T, volume V, and chemical potential μ. This method will be used in Chapter 5 to study phase coexistence of a model of Y-shaped particles on a hexagonal lattice. The algorithm is similar to the CMC however two additional types of moves are possible which are removal and

insertion of single particles. The acceptance rates for these moves are

$$a(N \to N + 1) = \min \left[\frac{V}{N+1} e^{\beta\mu} e^{-\beta(U(N+1)-U(N))} \right] \tag{2.18}$$

$$a(N \to N - 1) = \min \left[\frac{N}{V} e^{-\beta\mu} e^{-\beta(U(N+1)-U(N))} \right] \tag{2.19}$$

for insertion and removal of particles respectively. Through varying μ and T, two phase coexistence is found when the system fluctuates between the two densities of the respective phases. The two peak densities can be recorded for T and this process can be repeated for multiple T. To avoid performing numerous simulations, we use the standard method of histogram reweighting to approximate phase coexistence. There are also cases when the free energy barrier between two phases is rather large, and can cause long lived states in either phase as well as make it more difficult to transition from one phase to another. A combination of histogram reweighting and biasing enables the simulation to fluctuate between phases more easily, saving computation time and increasing accuracy.

2.5   Histogram Reweighting

Suppose one has performed a GCMC simulation for a certain T and μ, and determined a joint probability distribution $P_{w,\mu}(\rho, u)$. The probability distribution at a new T' and μ' can be estimated through

$$P_{w',\mu'}(\rho, u) = \frac{\exp[(\mu' - \mu)\rho N - (w' - w)uN]P_{w,\mu}(\rho, u)}{\sum \exp[(\mu' - \mu)\rho N - (w' - w)uN]P_{w,\mu}(\rho, u)} \tag{2.20}$$

This method of estimating new PDFs is of use to determine coexistence, which is reached when the areas under each density peak are equal. In other words, each phase is equally likely to be observed in the system. This method is also of use for determining coexistence at lower temperatures. In normal GCMC simulations, at low temperatures the free energy barrier between two phases becomes large and the average lifetime of phases is much longer due to the low probability of transitional states. We use the standard multicanonical Monte Carlo method, which is a biased

sampling technique, to avoid this slowdown. This is done by adding another proba-
bility to moves which is dependent on the density of the system such that densities
between the peaks of the two phases are more likely, thus encouraging transitioning
between phases. Since this density dependent probability is not detail balanced nor
is it in accordance with statistical mechanics, the systems recorded when using his-
togram reweighting are not truly generated according to their actual probabilities
of occurence. The density histogram must be corrected in accordance to the density
dependent probability and then those results are truly the ones of interest.

Instead of sampling from the usual Boltzmann distribution with a reduced Hamil-
tonian of $\overline{H}(\overrightarrow{r_i}) = \overline{H}_o + \mu N$, where $\overline{H}_o$ is the summation of interactions between
all molecules in units of kT, we introduce a new effective Hamiltonian $(\overline{H'}(\overrightarrow{\{r_i\}}))$
such that the new distribution is approximately uniform as a function of density,
eliminating the slowdown caused by the large free energy barrier between the two
phases.

The new Hamiltonian is of the form $\overline{H'}(\overrightarrow{\{r_i\}}) = \overline{H}(\overrightarrow{\{r_i\}}) + g(\rho)$, where $g(\rho)$ is
the dimensionless preweighting function which can be determined such that

$$P'(\rho) = \frac{1}{Z'} \prod \left\{ \int d\{r_i\} \right\} e^{-\overline{H'}(\overrightarrow{\{r_i\}})} \approx Constant. \qquad (2.21)$$

One choice of preweighting functions is such that $g(\rho) = ln(P(\rho))$. This ensures
that Eq. (2.21) is true. Since $P(\rho)$ is what we wish to determine from the simulation
itself, we approximate $P(\rho)$ using the histogram reweighting method prior to the
simulation. To unbias the $P'(\rho)$ determined from the GCMC simulation (using the
preweighting function), $P(\rho)$ can be determined by

$$P(\rho) = P'(\rho)e^{g(\rho)} \qquad (2.22)$$

This combination of histogram reweighting and biasing makes for more efficient
determination of phase diagrams due to the rapid fluctuations in the system. There
are numerous other methods to enhance the determination of coexistence points
including Gibbs ensemble simulation or "floppy" box method, as well as other tech-
niques to aid the simulation types described in this chapter including orientational

biasing and cluster algorithms. The simulation method used in Chapters 3 and 4 is the Canonical Monte Carlo method. Chapter 3 includes the calculation of the ensemble averages of cluster distributions, orientation correlation of interacting particles, and mononomer density. The Canonical Monte Carlo method was also executed to determine the second virial coefficient of Janus ellipsoids at varying temperatures. In Chapter 5 the Grand Canonical ensemble is implemented, as well as the process for histogram reweighting and biasing discussed.

Chapter 3

The Impact of Anisotropy and Interaction Range on the Self-Assembly of Janus Ellipsoids

3.1 Introduction

The self-assembly of anisotropic colloidal particles, whose interactions depend on both particle separation and relative orientation, is an important step in the creation of mesostructures that have a multitude of technological applications, including those in such fields as drug delivery and photonic crystals [49, 50, 51]. A prototype of such particles is the so-called "patchy" colloids that have been fabricated both experimentally and for use in computer simulations of self-assembly. By varying the number and distribution of patches on the surface of a particle, one can effectively tune the resulting shapes of aggregates to create useful structures [49, 52, 53]. The impact of particle anisotropy on the self-assembly process has been summarized by Glotzer and Solomon employing the concept of an anisotropy dimension that reflects particle patchiness and aspect ratio [54]. Nature also takes advantage of anisotropy in various protein molecules, whose self-assembly and morphology depend on anisotropy[55].

The Janus sphere, comprising two chemically dissimilar hemispheres, is perhaps the simplest, well-studied example of a patchy colloid [52, 56, 57]. Janus spheres have been fabricated by a variety of techniques [58, 59] and used, for example, to study particle interactions with cells [60] and to manufacture imaging probes [61] and sensors [62]. In addition, Monte Carlo simulation of these systems has led to a better understanding of the thermodynamics and morphologies associated with self-assembly [57, 63]. In particular, Hong *et al.* [64] showed that charged Janus spheres aggregate in clusters (as opposed to strings), a result that agrees well with experiment. In addition, Sciortino *et al.* [56] determined the gas-liquid portion of the phase diagram for a Kern-Frenkel[65] model of Janus spheres whose attractive interaction range is 0.5σ, where σ is the diameter of the sphere. Vissers *et al.* [66] subsequently determined the complete phase diagram for the same model of Janus spheres, with an interaction range of 0.2σ, focusing in particular on the nature of the crystal phases.

As indicated above, the introduction of anisotropy with the creation of patchy surfaces may expand the range of structural morphologies that can be produced via colloidal self-assembly. This might also be of relevance in describing the self-assembly of proteins with specific anisotropic interactions (e.g. hydrophobins[67] or micelle forming proteins[68]). For example, in recent Monte Carlo simulations of Janus ellipsoids using a modified square-well model, it was found that the size and structure of aggregates formed by self-assembly are dictated to a large extent by the ellipsoid aspect ratio [69] and that, by contrast with oblate spheroids, prolate spheroids form a variety of ordered cluster structures [70]. Despite significant progress in recent years in relating colloidal characteristics to the resulting aggregate morphology, a complete picture of the impact of anisotropy and interaction range on self-assembly is still lacking. This incompleteness is due, at least in part, to the difficulty in equilibrating aggregating systems having both translational and rotational degrees of freedom using computer simulation. Thus, most studies to date have considered simplified interactions with ranges that are longer than those found experimentally.

In this paper, we employ Monte Carlo simulation to assess the roles of these

characteristics in self-assembly using a simplified spheroidal model of a Janus colloid. More specifically, for a relatively short-ranged interaction that is consistent with experimentally realizable systems, we investigate the formation of single-layer and multilayer aggregates for ellipsoidal particles and, in so doing, identify a "micelle" transition temperature. By comparing our results with those established for Janus spheres, we highlight the impact of colloidal characteristics on this transition and on the propensity to form aggregates.

As we have investigated the aggregation of Janus ellipsoids in two earlier studies [69, 70], it is important to highlight what is new in this study. First, in this work we extend previous observations of clustering to identify a micellization temperature below which substantial clustering occurs. This is a substantial extension that requires the compilation of equilibrium cluster frequencies and the assessment of the dependence of equilibrium monomer density on particle density. Second, to establish phase boundaries and to determine the dependence of the critical temperature on the interaction range, we construct here an approximate phase diagram for our system. The phase diagram is also useful to establish that, for most of the particle densities considered here, the system is in a gas phase comprising a spectrum of n-mers. Finally, it should be noted that the use of a relatively short-ranged interaction here, as compared with earlier studies, complicates the simulations as it leads to very long equilibration times. (Indeed, in the study of Janus spheres with the same interaction range as ours[66], the authors found it virtually impossible to equilibrate the fluid at low temperatures.) Thus, the computational overhead in this study greatly exceeds that of our previous investigations of Janus ellipsoids, a necessary cost to model interactions that are more consistent with experiment.

3.2   Simulation Methodology

The simulation procedure employed here has been described in some detail elsewhere [69]; hence, we merely outline the main features below. We model the Janus particles as spheroids having principal axes given by $a \neq b = c$, with a particle being classified

as oblate (prolate) if the corresponding aspect ratio $\epsilon = a/b$ is less (greater) than unity. For convenience, we denote the longer axis as $\sigma = max\,(a, b)$. To describe an anisotropic system, we extend the patchy model introduced by Kern and Frenkel [65] to our geometry.

Consider two interacting spheroids, i and j, with a center-to-center displacement $\mathbf{r}_{ij}$ and patch vectors $\mathbf{u}_i$ and $\mathbf{u}_j$, respectively, as shown in Fig. 1. In this model, two particles separated by a distance r_{ij} interact with an orientation-dependent pair potential (similar to a square well) given by $U_{ij} = U f(\mathbf{r}_{ij}, \mathbf{u}_i, \mathbf{u}_j)$, where

$$
U = \begin{cases} \infty, & \text{if particles overlap} \\ -U_0\, \Theta\,(\sigma_{ij} + w\sigma - r_{ij}), & \text{otherwise} \end{cases} \tag{3.1}
$$

U_0 is the well depth, Θ is the Heaviside function, and w is the width of the well. The orientation function is given in terms of $\mathbf{u}_i$ and $\mathbf{u}_j$ by

$$
f(\mathbf{r}_{ij}, \mathbf{u}_i, \mathbf{u}_j) = \begin{cases} 1, & \text{if } |\mathbf{u}_i \cdot \hat{\mathbf{r}}_{ij}| \geq \cos\delta \\ 0, & \text{otherwise} \end{cases} \tag{3.2}
$$

Following the approach of Berne and Pechukas [71], in writing Eq. (3.1) we have adopted a Gaussian model to represent approximately the attractive interaction of the ellipsoids. In this approach, σ_{ij} is an orientation-dependent interaction length given by

$$
\sigma_{ij} = 2b \left[1 - \frac{\chi}{2} \left(\frac{(\mathbf{u}_i \cdot \hat{\mathbf{r}}_{ij} + \mathbf{u}_j \cdot \hat{\mathbf{r}}_{ij})^2}{1 + \chi \mathbf{u}_i \cdot \mathbf{u}_j} + \frac{(\mathbf{u}_i \cdot \hat{\mathbf{r}}_{ij} - \mathbf{u}_j \cdot \hat{\mathbf{r}}_{ij})^2}{1 - \chi \mathbf{u}_i \cdot \mathbf{u}_j} \right) \right]^{-1/2}, \tag{3.3}
$$

where the asymmetry parameter $\chi = (\epsilon^2 - 1)/(\epsilon^2 + 1)$ [71].

We employ Monte Carlo (MC) simulation in the Canonical (NVT) ensemble to study the equilibrium aggregation of the Janus particles. Our simulations begin with a gas of randomly distributed monomers. Both standard Metropolis sampling and, in some cases, cluster sampling, the latter involving the translation and rotation of aggregates, were used to generate the sequence of subsequent configurations for a system comprising N particles ranging from roughly 280 to 580 in a periodic, cubic

simulation cell with length l ranging from 18 to 72σ. The cluster algorithm[72] is an extension of similar sampling strategies [73] used to mitigate critical slowing down in spin systems, and was used in this context to expedite equilibration in systems with low densities.

For convenience, we report lengths in units of σ and energy in units of U_0 and, given our focus on highly anisotropic systems with a short-ranged attractive interaction, we choose $w = 0.2$ and $\epsilon = 0.6$. To assess the degree of aggregation, we calculate several quantities including the monomer density as a function of particle density and the frequency of aggregates of a given size. As equilibration is often slow, particularly for small N, we employ long runs having typically 1×10^8-5×10^8 MCS. Moreover, our results are typically averaged over 2500 independent equilibrium configurations to obtain statistically meaningful results. The short interaction range leads to very long equilibration times, making the results presented in the next section computationally expensive to obtain, particularly for the systems of low temperature and density.

3.3 Results

3.3.1 Cluster Densities

As indicated above, our aim here is to assess the roles of interaction range and anisotropy on colloidal self-assembly for Janus particles. The degree of aggregation in our system is conveniently quantified in terms of an n-mer density, ρ_n that varies as a function of temperature, T, and particle density, ρ. Consider first the monomer density, ρ_1, as a function of ρ for a range of T, as shown in Fig. 3.2. For reference, the ideal gas result, which should describe a system of non-interacting monomers at sufficiently high temperature, is also shown. As noted by Sciortino *et al.*[57], the dependence of ρ_1 on ρ is useful in locating (approximately) the micellization temperature. More specifically, those regimes for which ρ_1 is rather insensitive to ρ indicate that the addition of particles results in the formation of aggregates. Using this criterion, it is reasonable to estimate from the figure that a transition occurs

at $T \approx 0.21$. As in the case for the Janus spheres[57], this transition temperature is close to our estimate of the gas-liquid critical temperature T_c for the system, as we discuss later. Figures 3a-d shows some typical cluster morphologies resulting from self-assembly. We note that a visual examination of equilibrium cluster morphologies at this temperature, as shown for example in Fig. 3c, for aggregates comprising of the order of 30 or more particles suggests that the formation of multilayer, rather than single-layer, structures is favored. The prevalence of multilayer structures for larger aggregates is highlighted in Fig. 3d, which shows a cut away of the 30-particle aggregate shown in Fig. 3c. This aggregate is seen to have the classical structure of a vesicle.

To investigate the type and frequency of aggregates resulting from self assembly, we monitor the equilibrium cluster sizes, s, in our system as a function of T and ρ. For concreteness, we shall regard aggregates with $s \simeq 10$ as single-layer structures and those with $s > 20$ as multi-layer structures. As will be seen below, this classification scheme, while somewhat arbitrary, is quite useful in characterizing observed aggregates. (There is, of course, an intermediate regime in which a nominally single-layer structure surrounds a very small number of particles.) A summary of the results is given by the cluster-size histogram, $N\left(s\right)$, shown in Fig. 3.4. As is evident from the figure, at $\rho = 0.001$, there is no peak for $s \approx 10$ (i.e., signifying single-layer structures), and most structures are either monomers or multilayer clusters, the latter with $s > 20$. The aforementioned intermediate regime is also present for $s \approx 20$. At higher particle densities a relatively few single-layer structures form in addition to the more complex aggregates. This behavior can be understood by examining effective interactions in this system as a function of well width, w, and the asymmetry parameter, χ, as discussed in section III C. Some insight into the structure of these aggregates can also be obtained by examining orientational correlations between interacting particles.

3.3.2 Orientational Correlation Function

Consider the orientational ordering associated with particle aggregates, as quantified by an orientational correlation function between patch normal vectors, $P(\mathbf{u}_1 \cdot \mathbf{u}_2)$. This quantity embodies orientational correlations between particles that are within the interaction range of the potential. In a state of total disorder this correlation function will be flat as every relative orientation is equally probable whereas, in an ordered state, distinct peaks indicate preferred relative orientations. In particular, peaks that are predominantly at $\mathbf{u}_1 \cdot \mathbf{u}_2 \approx 1$ are associated with particles whose patch normals are nearly parallel, as is characteristic of a single-layer structure in which, as is the case here, the interaction range is relatively short. For such a structure, nearest-neighbor particles within the interaction range tend to be bonded side-to-side, and therefore their patch normal vectors are nearly parallel. On the other hand, peaks predominantly at $\mathbf{u}_1 \cdot \mathbf{u}_2 \approx \pm 1$ are indicative of a multilayer structure. As can be seen in Fig. 3.5, there are no significant differences in the double-peak structure of the correlation function for temperatures $T = 0.19 - 0.21$. In studies for $T \geq 0.23$ it was found that $P(\mathbf{u}_1 \cdot \mathbf{u}_2)$ was essentially featureless and decreasing with increasing $\mathbf{u}_1 \cdot \mathbf{u}_2$, suggesting that neither single-layer nor multilayer aggregates were present and that, therefore, $T = 0.23$ is greater than the transition temperature.

3.3.3 Second Virial Coefficient

A quantitative measure of the propensity for aggregation may be obtained by calculating the second virial coefficient. Indeed, the magnitude of the particle interactions over a range of temperatures, T, is conveniently characterized by the second virial coefficient

$$B_2(T) = \frac{1}{2V} \frac{1}{(4\pi)^2} \int d^3 r_1 d^3 r_2 d^3 u_1 d^3 u_2 \, [1 - \exp(-\beta U_{12}(\mathbf{r}_{12}, \mathbf{u}_1, \mathbf{u}_2))], \quad (3.4)$$

where $\beta = 1/k_B T$ and k_B is Boltzmann's constant. More specifically, a negative value for the virial coefficient indicates a propensity for aggregation, while the converse is true for a positive value [74]. To explore the variation of $B_2(T)$ with the well width, w, and aspect ratio, ϵ, it is useful to obtain an approximation for this

26

quantity. This can be done by employing an analytical expression for the second virial coefficient in a d-dimensional Gaussian model of hard ellipsoids developed by Cuesta and Tejero [75]. Generalizing their expression to a square-well potential with effective width, w, and using a spherical approximation for the integration over patch orientations, one obtains for the normalized virial coefficient

$$\frac{B_2(T)}{B_2^{hs}} \approx \frac{1}{2} \left(1 + \frac{\sin^{-1} \chi}{\chi (1 - \chi^2)^{1/2}} \right) \sqrt{\frac{1+\chi}{1-\chi}} \left[1 + \frac{1}{4} \left((1+w)^3 - 1 \right) \left(1 - e^{\beta U_0} \right) \right],$$

(3.5)

where $B_2^{hs} = 2\pi\sigma^3/3$ is the corresonding coefficient for hard spheres. It should be noted that, for asymmetry parameter $\chi = 0$ one obtains an exact expression for Janus spheres, i.e.,

$$\frac{B_2(\chi = 0, T)}{B_2^{hs}} = 1 + \frac{1}{4} \left((1+w)^3 - 1 \right) \left(1 - e^{\beta U_0} \right),$$

(3.6)

and that, for small χ, $B_2(\chi, T)/B_2(\chi = 0, T) \approx 1 + \chi$.

The normalized second virial coefficient is shown in Fig. 3.6 for two well widths, $w = 0.2$ and $w = 0.5$, and aspect ratio $\epsilon = 0.6$ ($\chi = -0.47$). For comparison, approximations to this coefficient obtained from Eq. (3.5) for other values of the width and shape parameters are also shown. The integration indicated in Eq. (3.4) was done numerically using the Monte Carlo method. It can be seen from the figure that the approximation to the virial coefficient agrees well with the Monte Carlo results. Clearly, a decrease in the well width, w, leads to a decrease in the normalized virial coefficient, $B_2(T)/B_2^{hs}$, and, therefore, a decrease in the propensity for aggregation.

This behavior is highlighted in Fig. 7, which shows $B_2(T)/B_2^{hs}$ as a function of both well width, w, and the magnitude of the asymmetry parameter, $|\chi|$, as obtained from Eq. (3.5) for ellipsoids with $\chi < 0$. From the figure it is evident that the normalized second virial coefficient also decreases with increasing $|\chi|$ (for $\chi < 0$), indicating that, for the same well width and temperature, oblate particles are less likely to aggregate as compared to spherical particles. This steric effect may explain the observation that few single-layer structures form for small ρ. The lack of such structures for spheroidal particles also makes sense from geometrical considerations.

In particular, spheroidal particles will align preferentially face-to-face, rather than in the side-to-side configuration associated with single-layer structures, to increase the number of neighbor interactions. A preference for face-to-face alignment therefore inhibits the formation of single-layer structures. This behavior can be seen in Fig. 3.5, which shows a larger probability for face-to-face alignment (although no well-defined peak) as opposed to side-to-side alignment for $T = 0.23$.

3.3.4   Phase Diagram

Finally, to put our results in context, we estimate the phase diagram of our system. As it is computationally too expensive to determine the phase diagram for this short-range model, we use the extended law of corresponding states as proposed by Noro and Frenkel originally[76] for spherically symmetric isotropic particles with short range attractive forces (such as in our case). This so-called law states that the thermodynamic properties become insensitive to the details of the potential and depend only on the value of the second virial coefficient B_2 and the density. This was then extended[77] to include certain types of non-spherical potentials (patchy models) when the particles interact via short-ranged small-angular amplitude patchy interactions (so that the condition of only one bond per patch is fulfilled). We use this B_2 scaling here as a way to obtain a rough estimate of the phase diagram for this system of Janus spheroids. More specifically, the phase diagram for Janus spheres having $w = 0.5$ that was calculated by Sciortino et al. [10] using temperature as the vertical axis is replotted using the second virial coefficient for the spherical Janus particles as the vertical axis. This requires calculating $B_{2sphere}(T)$ for each relative temperature and density point of the phase diagram of Janus spheres using Eq. (3.6). Then, we determine $B_{2spheroid}(T)$ via Monte Carlo integration for the Janus spheroid system studied here. From equating the B_2 values of the different systems, the points on the phase diagram for the spheroids corresponding to those for the spheres have the same values for $B_2(T)$.

The phase diagram resulting from this scaling procedure is shown in Fig. 8a. In Fig. 8b we present the phase diagram for Janus spheres determined by Sciortino

et al. [57] that was used in the rescaling described above. Upon comparing this phase diagram with that in Fig. 8a, it is clear that they are qualitatively similar. We note, however, that a more detailed comparison is difficult in this case since the very narrow temperature range employed here means that the rescaling used varies little with temperature. As expected, the critical temperature $T_c \approx 0.21$ is significantly lower than that found for the aforementioned Janus spheres having $w = 0.5$ [10] owing to the shorter interaction range here. For most of the range of temperatures and particle densities explored here, our system is in a gas phase containing a spectrum of n-mers. Although this rough estimate of the phase diagram is only meant as a guide to place the results of our cluster aggregation study into context, its overall shape makes sense. Namely, as noted by Sciortino[10], the coexistence gas density here increases progressively on cooling, approaching the coexisting liquid density. This is in contrast to simple fluids whose coexisting gas density decreases with cooling. Also in a simple liquid, gas-liquid coexistence results due to a balance between the gas and liquid free energies. The lower energy of the liquid phase is compensated by a larger entropy of the gas phase, which is acquired by significantly increasing the volume per particle. The unusual behavior observed for Janus spheres (and predicted to occur for our spheroids) comes about in a completely different way. As argued by Sciortino et al. [10] the gas becomes the energetically stable phase (due to the formation of orientationally ordered aggregates, micelles and vesicles) and the liquid phase instead is stabilized by the larger orientational entropy of the particles. Since our results for the formation of aggregates as one lowers temperature are similar to that for Janus spheres, we believe our rough estimate of the phase diagram is qualitatively correct.

Another indication of the approximate validity of the diagram can be seen by considering the average energy as a function of the temperature at a density of 0.001. The derivative of this energy with respect to the temperature gives the specific heat of the system (C_V). There is a peak in C_V, similar to what one would see near a gas-liquid critical point. The peak is at $T \approx 0.21$, which is consistent with that estimated by B_2 scaling. In addition, Sciortino *et al.* [56] determined the gas-liquid portion of the phase diagram for a Kern-Frenkel[65] model of Janus spheres whose

attractive interaction range is 0.5σ, where σ is the diameter of the sphere. They also addressed the issue of the relation between the gas-liquid phase coexistence and the process of micelle formation in the gas phase. (In such a case the gas phase is regarded as a collection of finite size aggregates, including micelles, and the liquid phase is considered to be an infinite size aggregate.) They found that the gas-liquid phase separation curve was characterized by a gas-liquid critical point and a micellar phase within the gas region at temperatures below the critical point. This micelle-rich gas phase coexists with a dense, fully connected liquid phase. One last point is worth noting. It would appear from our rough estimate of the phase diagram that our simulation for T in the range of $0.20 - 0.21$ and density approximately 0.2 could be in the phase separation region. However, we saw no such phase separation in this case, suggesting that the real coexistence curve is to the right of this region.

3.4   Discussion and Conclusions

We employed Monte Carlo simulation to characterize the formation of aggregates in a spheroidal model of a colloid having a relatively short-ranged interaction. An analysis of the equilibrium cluster size distribution for this system shows that aggregation occurs over a range of particle densities. However, unlike colloidal systems with longer ranged interactions, this system does not form single-layer structures below a transition temperature at low density; rather, larger clusters comprising $20 - 40$ particles are formed. This absence of "micellization" at low densities was interpreted in terms of the behavior of the second-virial coefficient as a function of interaction range and particle eccentricity. In addition, an examination of the orientational correlation function indicated that substantial orientational ordering occurs in the low-temperature, low- density regime. Thus, we conclude that the absence of a micellization temperature in the current study is attributed to the short interaction range of the potential and the spheroidal geometry of the particles.

From this and a previous investigation [78], it is clear that one potential application of Janus particle self assembly is the development of encapsulation systems.

Encapsulation systems are technologically relevant and can be used, for example, in specific drug targeting for the treatment of illnesses and for controlling the drug release time [79, 80, 81]. Our work indicates that the degree of encapsulation may be fine tuned by varying particle shape. In this chapter we have only considered a limited range of parameter space. It ought to be possible to optimize the range of particle interactions and particle aspect ratios to achieve a desired encapsulation morphology. The identification of a range of parameter space that is useful for encapsulation will be the subject of Chapter 4.

3.5 Acknowledgements
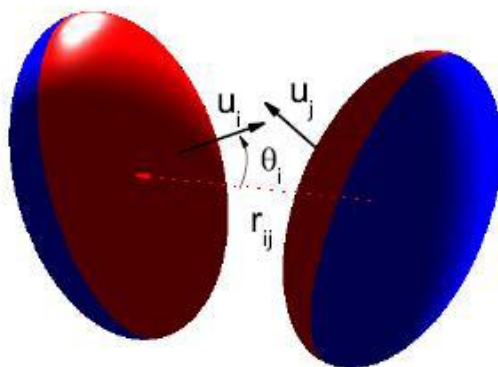
Figure 3.1: A schematic showing two interacting spheroids having a center-to-center displacement $\mathbf{r}_{ij}$ and patch vectors $\mathbf{u}_i$ and $\mathbf{u}_j$. The attractive and (hardcore) repulsive surfaces are shown in red and blue, respectively. Reprinted with permission from (Liu, Y.; Li, W.; Perez, T.; Gunton, J. D.; Brett, G. Self-Assembly of Janus Ellipsoids. Langmuir 2012, 28, 3-9). Copyright (2012) American Chemical Society.
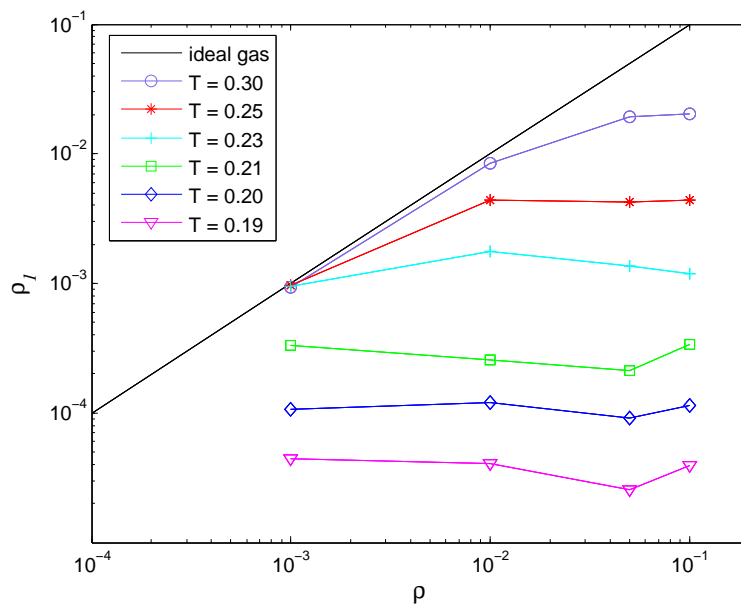
Figure 3.2: The monomer density, ρ_1, as a function of ρ for a range of T. For reference, the ideal gas result (solid line) is also shown. From this figure one can reasonably estimate that a transition occurs at $T \approx 0.21$.

(a) size = 4   (b) size = 9   (c) size = 30

(d) size = 30 internal view
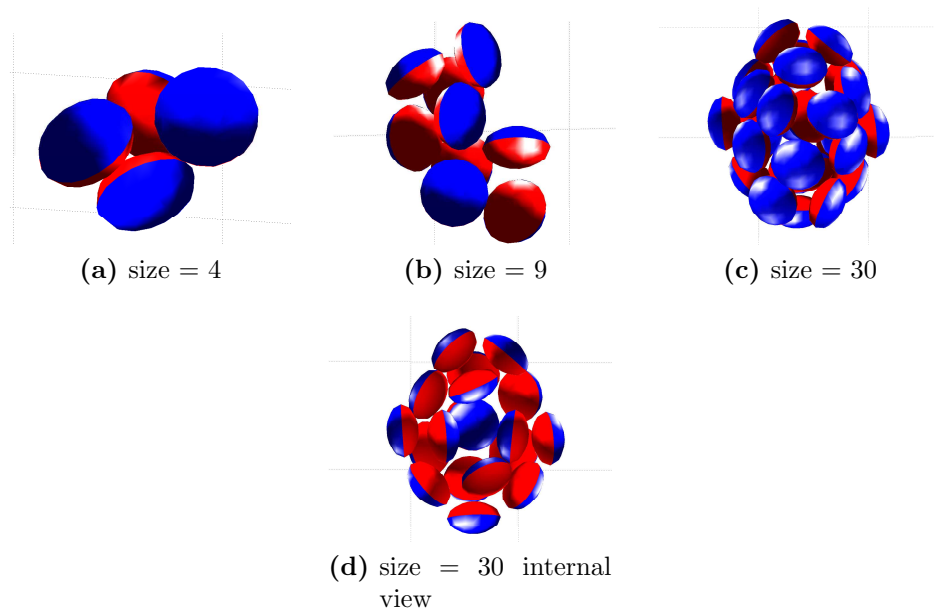
Figure 3.3: a-c.) Typical configurations of varying cluster sizes for systems with $\epsilon = 0.6$ and $w = 0.2$. d.) A cut away of the 30-particle aggregate shown in (c). The prevalence of multilayer structures is highlighted here
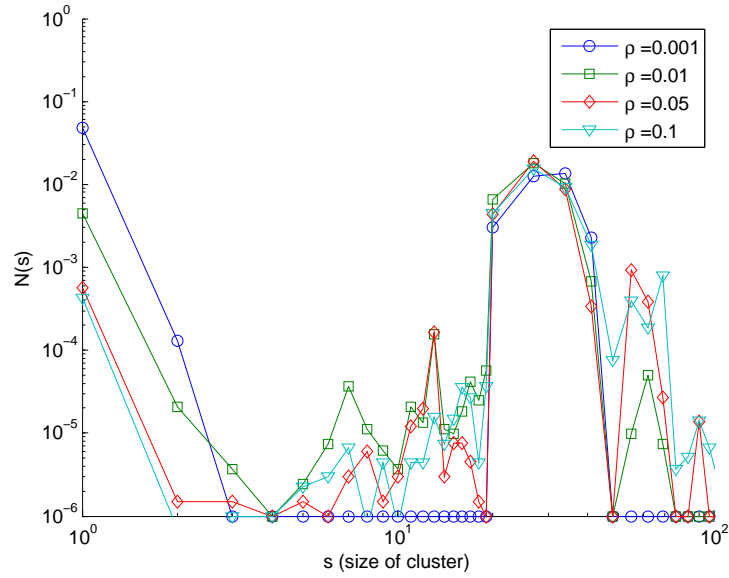
(a)
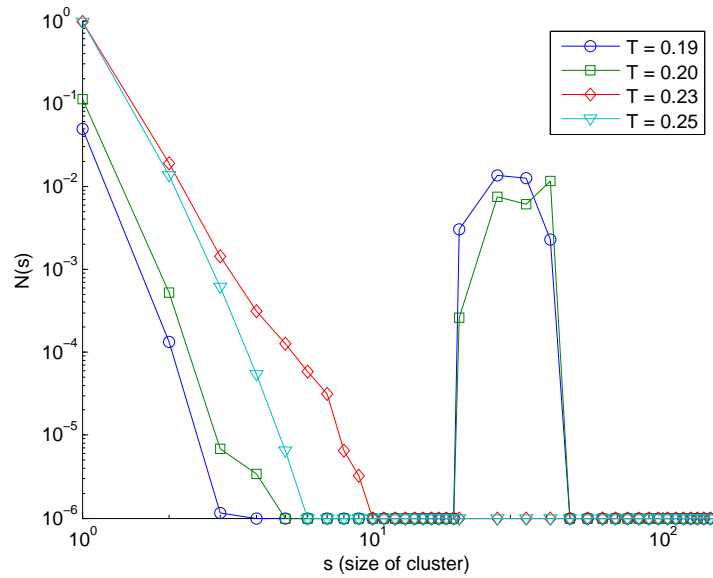
(b)

Figure 3.4: a.) The equilibrium cluster size distribution, $N(s)$, as a function of cluster size for $T = 0.19$ and $\rho = 0.001, 0.01, 0.5,$ and 0.1. b.) The equilibrium cluster size distribution, $N(s)$, as a function of cluster size for $\rho = 0.001$ and multiple temperatures. For both a) and b) $N(s)$ has been normalized such that $\sum_s sN(s) = 1$. The maximum error found in N(s) based on ≈ 2500 measurements is on the order of 10^{-4}.
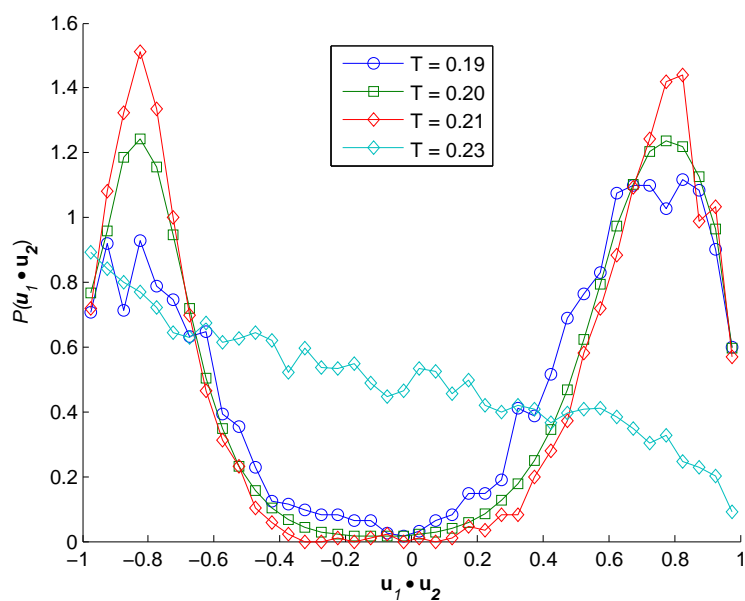
Figure 3.5: The distribution of orientation correlation over all pairs of bonded spheroid particles $P(\mathbf{u}_1 \cdot \mathbf{u}_2)$ is normalized such that $\sum_{\mathbf{u}_1 \cdot \mathbf{u}_2} P(\mathbf{u}_1 \cdot \mathbf{u}_2) = 1$. Peaks that are predominantly at $\mathbf{u}_1 \cdot \mathbf{u}_2 \approx 1$ are characteristic of a single-layer structure in which, as is the case here, the interaction range is relatively short. Peaks predominantly at $\mathbf{u}_1 \cdot \mathbf{u}_2 \approx \pm 1$ are indicative of a multilayer structure.
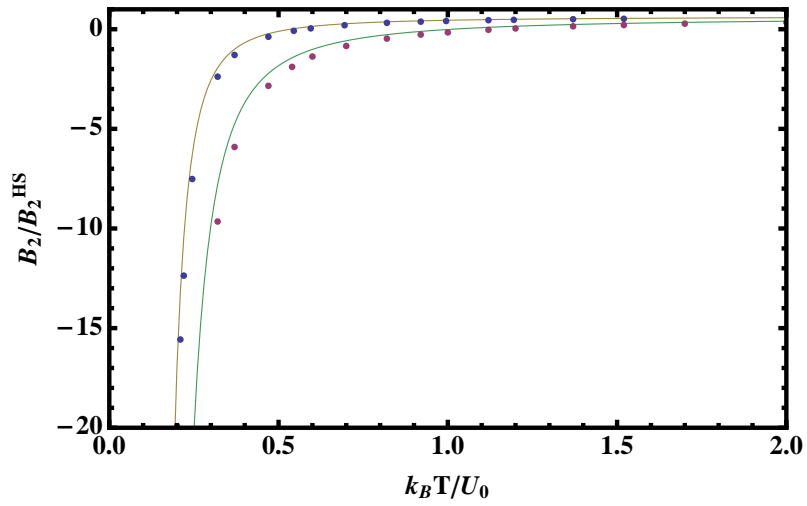
Figure 3.6: a.) The normalized second virial coefficient, $B_2\left(T\right)/B_2^{hs}$, versus the reduced temperature, k_BT/U_0, for both well widths $w = 0.2$ (blue dot) and $w = 0.5$(magenta dot) and aspect ratio $\epsilon = 0.6$ ($\chi = -0.47$), and approximations to this coefficient obtained from Eq. (3.5) (solid lines). The asymmetry parameter $\chi = \left(\epsilon^2 - 1\right)/\left(\epsilon^2 + 1\right)$.
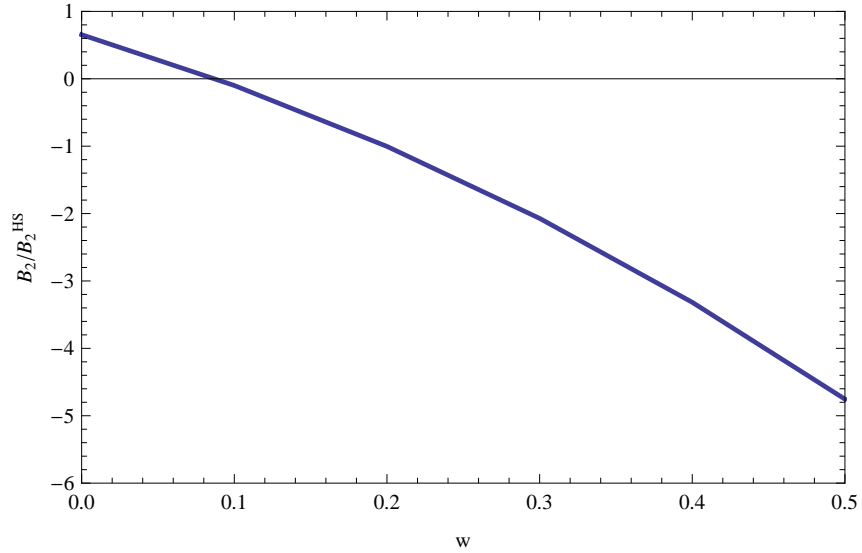
(a)
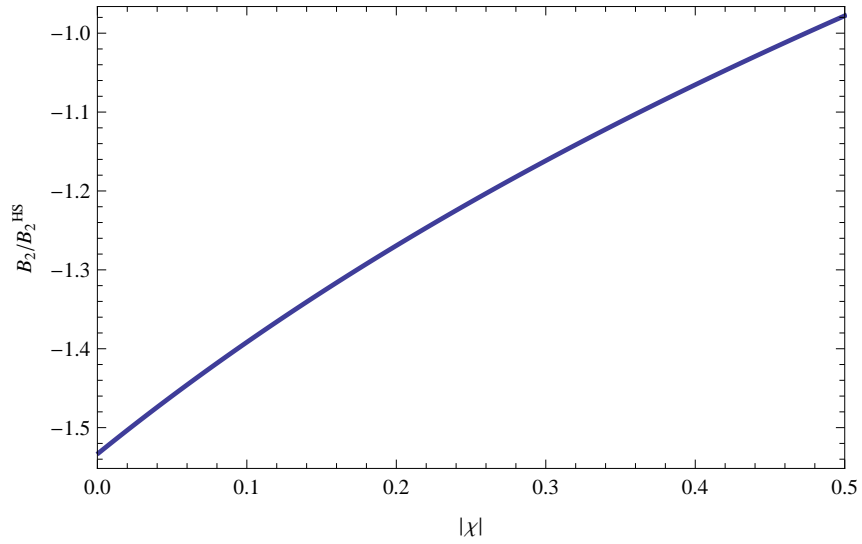
(b)

Figure 3.7: a.) The normalized virial coefficient, $B_2\left(T\right)/B_2^{hs}$, versus well width, w, for asymmetry parameter $\chi = -0.47$ at reduced temperature $k_B T/U_0 = 0.37$, as determined from Eq. (3.5). b.) $B_2\left(T\right)/B_2^{hs}$ versus $|\chi|$ for $w = 0.2$ at $k_B T/U_0 = 0.37$, as determined from Eq. (3.5). From these results one infers that oblate particles are less likely to aggregate as compared to spherical particles.
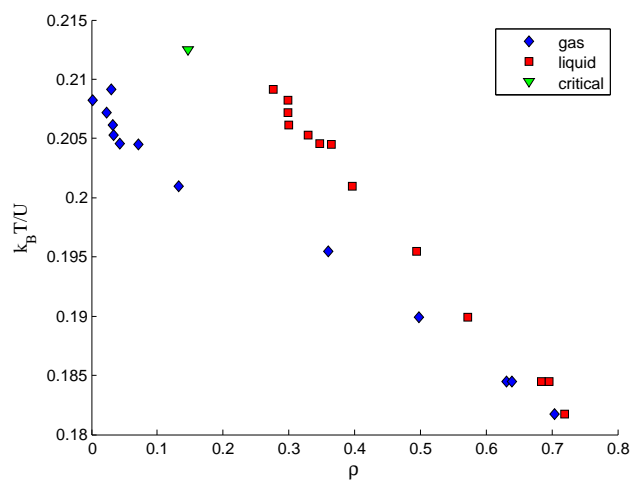
(a)
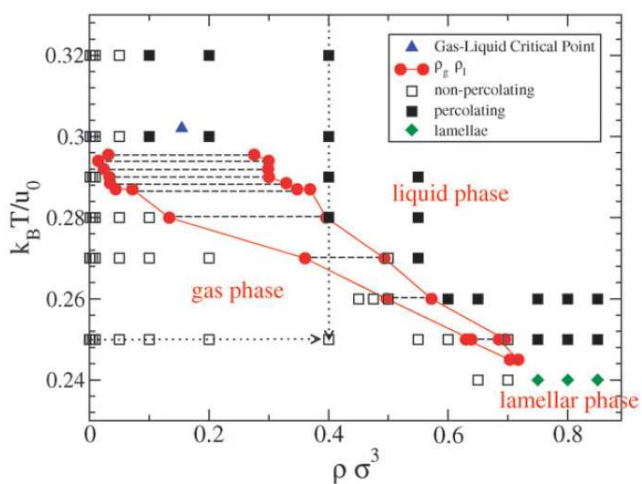
(b)

Figure 3.8: a.) The approximate phase diagram for ellipsoids having well width, $w = 0.2$, and asymmetry parameter, $\epsilon = 0.6$, ($\chi = -0.47$) as obtained from B_2 scaling. b.) The corresponding phase diagram for Janus spheres ($\chi = 0$). Reprinted with permission from (Sciortino, F.; Giacometti, A.; Pastore, G. A Numerical Study of One-Patch Colloidal Particles: From Square-Well to Janus. *Phys. Chem. Chem. Phys.* **2010**, *12*, 11869-11877.) Reproduced by permission of the PCCP Owner Societies.

http://dx.doi.org/10.1039/C0CP00504E

Chapter 4

Selective Encapsulation by Janus Particles

4.1 Introduction

Microencapsulation technology is a scientifically intriguing and technologically important topic of current research. [82, 83, 84] In general, microencapsulation can be used to protect the guest object being encapsulated from the outside environment and, hence, increase the stability and lifetime of the guest. Moreover, microencapsulation can be employed to control the rate of release of the guest substance. As a result, the capsule systems produced at the micro-/nano-meter scale have broad applications in various fields, such as pharmaceuticals [82, 85], materials science [86, 87], the chemical [83, 88] and food industries [84, 89, 90], etc. For instance, the micron capsule functioning as carriers in drug delivery systems can be used not only to overcome the transport problems of the drugs (such as limited water solubility, stability and high systemic toxicity etc) [85, 91], but also to achieve targeted drug delivery [92, 91, 93]. Moreover, the ability to develop controlled-release delivery makes the capsule system an ideal choice for applications in drug therapy. [94, 95]

A range of approaches to achieve encapsulation has been proposed and implemented in recent years. [96, 97, 95, 82, 98, 99] Among these approaches, those that

promote self-assembly into capsules under a specific set of conditions constitute an important class of encapsulation strategies. These self-assembling systems mainly consist of amphiphilic molecules and macromolecules, such as lipids and amphiphilic block copolymers. [92, 97, 95] The size of the liposomes or vesicles formed in these systems spans from tens of nanometers to a few microns. This provides a versatile platform for smart materials, for which the release or uptake of their payload is controlled upon introducing external stimuli, such as a change in temperature, pH, oxidation/reduction, etc. [94, 100] Nowadays, due to recent advances in particle synthesis, a new type of amphiphilic particle, the so-called Janus particle, has been broadly produced. [101, 102, 103] Janus particles are colloidal particles whose two hemi-surfaces are coded differently in their chemical or physical properties. A series of experimental and numerical investigations has been performed to investigate the nature of the Janus particles self-assembly. [104, 105, 106, 107, 108, 109, 110, 111, 112] Moreover, the micelle and vesicle structures formed by different Janus particles have been studied. [105, 107, 108, 109, 110, 111]

In a previous report, [113] we proposed a new encapsulation system, consisting of Janus oblate spheroids and isotropic spheres, in which the spheroids act as the encapsulating agents and the spheres as encapsulated guests. As in the case of self-assembling lipids and block copolymers described above, the ability to form shells by self-assembly makes the Janus spheroid a good candidate for an encapsulating agent. Given the length scales involved, one can envision encapsulation length scales on the order of microns. Moreover, the voids created in the Janus spheroidal shells by packing have the potential to make the capsules porous, a desirable feature for mesoporous/macroporous materials which have a wide range of applications, such as in catalysis and controlled drug delivery systems etc. [114] In an initial study at given simulation conditions, we found that for a specific guest sphere whose diameter equals the major axis length of the spheroids, the encapsulation by the Janus spheroids is highly efficient. This is particularly true for an aspect ratio equal to 0.6. [113]

In this chapter, we continue our study of this new proposed encapsulation system and further investigate the associated thermodynamics of self-assembly. The

41

phase diagram of this blended system remains unknown, and our main focus is on the encapsulation properties. Hence, for simplicity, we limit ourselves to a narrow range of simulation conditions, i.e., to the low-temperature and low-density regime. Furthermore, the system has more spheroids than spheres to ensure encapsulation sufficiency. In our investigation, we first vary the particle interaction range and the temperature to study the system's response and stability upon changing the environmental conditions. We then vary separately the size of the guest spheres and the strength of the agent-guest interaction to study the selectivity of the encapsulation with regard to different guest objects. This systematic study reveals some interesting aspects of the encapsulation behavior of the Janus spheroids.

4.2 Model and Simulation Method

In this study, we utilize the same model for the encapsulation system as proposed in the earlier work. [113] In the system, the encapsulating agents are Janus spheroids and the encapsulated guests are isotropic spheres. A Janus spheroid is defined as a hard-core spheroidal particle covered with a hemi-surface patch along its principal axis whose semi-diameter is $\sigma_\parallel$. The two equal semi-diameters are denoted as $\sigma_\perp$ and the aspect ratio $\varepsilon \equiv \sigma_\parallel/\sigma_\perp$. We use a 'quasi-square-well' patch model to describe the interaction between two objects, denoted by i and j, whose potential energy $U_{ij} = U(r_{ij})f(\hat{r}_{ij}, \hat{n}_i, \hat{n}_j)$. [113] The angular-dependent part of this potential is given by

$$f(\hat{r}_{ij}, \hat{n}_i, \hat{n}_j) = \begin{cases} 1 & \text{if } \hat{n}_i \cdot \hat{r}_{ij} \leq 0, \hat{n}_j \cdot \hat{r}_{ij} \geq 0 \\ 0 & \text{otherwise,} \end{cases} \tag{4.1}$$

where $\hat{r}_{ij}$ is the unit vector along the center-to-center direction vector $\vec{r}_{ij} \equiv \vec{r}_i - \vec{r}_j$ and $\hat{n}_i$ and $\hat{n}_j$ are the patch orientation vectors. Note that the isotropic sphere is a special case for which the patch orientation is set to be opposite to the separation vector, so that the angular dependent criterion is always satisfied for the sphere.

The separation-dependent potential $U(r_{ij})$ is given as

$$U(r_{ij}) = \begin{cases} \infty & \text{if particles overlap} \\ -u^* H(\sigma_{ij} + w\sigma_0 - r_{ij}) & \text{otherwise,} \end{cases} \qquad (4.2)$$

where the well depth u^* equals u_{ee}, u_{es} or u_{ss} for spheroid-spheroid, spheroid-sphere or sphere-sphere interactions, respectively. In addition, w is the well width and σ_0 is the unit of length. The Heaviside step function $H(\sigma_{ij} + w\sigma_0 - r_{ij})$ cuts off the interaction for a center-to-center distance greater than $\sigma_{ij} + w\sigma_0$. Consequently, this model describes two types of interactions, i.e., attraction between the hemi-surface patches and the spheres and a hard-core repulsion for the other contacts.

σ_{ij}, the orientation-dependent range, is generated from a Gaussian overlap model of Berne and Pechukas. [115] In particular, the spheroidal Gaussian is defined by $G(\vec{r}) = exp(-\vec{r} \cdot \boldsymbol{\gamma}^{-1} \cdot \vec{r})$, where $\vec{r}$ is the three-dimensional position vector and the range matrix $\boldsymbol{\gamma} = (\sigma_{\parallel}^2 - \sigma_{\perp}^2)\hat{n}\hat{n} + \sigma_{\perp}^2 \boldsymbol{I}$. In this last expression, $\hat{n}$ is the unit vector along the principal axis of $\sigma_{\parallel}$ and $\boldsymbol{I}$ is the unit matrix. In the overlap model, the interaction potential between two spheroids is a convolution of two Gaussians, which is written as

$$V(\hat{n}_i, \hat{n}_j, \vec{r}_{ij}) \sim |\boldsymbol{\gamma}_i|^{-1/2}|\boldsymbol{\gamma}_j|^{-1/2} \int d\vec{r} exp[-\vec{r} \cdot \boldsymbol{\gamma}_i^{-1} \cdot \vec{r} - (\vec{r} - \vec{r}_{ij}) \cdot \boldsymbol{\gamma}_j^{-1} \cdot (\vec{r} - \vec{r}_{ij})]$$
$$\sim |\boldsymbol{\gamma}_i + \boldsymbol{\gamma}_j|^{-1/2} exp[-\vec{r}_{ij} \cdot (\boldsymbol{\gamma}_i + \boldsymbol{\gamma}_j)^{-1} \cdot \vec{r}_{ij}] \qquad (4.3)$$

This potential can be expressed in the simple form

$$V(\hat{n}_i, \hat{n}_j, \vec{r}_{ij}) = \epsilon(\hat{n}_i, \hat{n}_j) exp[-r_{ij}^2/\sigma^2(\hat{n}_i, \hat{n}_j, \hat{r}_{ij})]. \qquad (4.4)$$

where $\epsilon(\hat{n}_i, \hat{n}_j)$ and $\sigma(\hat{n}_i, \hat{n}_j, \hat{r}_{ij})$ are orientation-dependent strength and range parameters, respectively. [115] By extending the mathematical development in the original paper (Ref. [115]), one can derive an explicit form for $\sigma(\hat{n}_i, \hat{n}_j, \hat{r}_{ij})$, namely

$$\sigma(\hat{n}_i, \hat{n}_j, \hat{r}_{ij}) = (\sigma_{i\perp}^2 + \sigma_{j\perp}^2)^{\frac{1}{2}} \left[1 - \left(\frac{\lambda_i(\hat{r}_{ij} \cdot \hat{n}_i)^2 - 2\lambda_i\lambda_j(\hat{r}_{ij} \cdot \hat{n}_i)(\hat{n}_i \cdot \hat{n}_j)(\hat{r}_{ij} \cdot \hat{n}_j) + \lambda_j(\hat{r}_{ij} \cdot \hat{n}_j)^2}{1 - \lambda_i\lambda_j(\hat{n}_i \cdot \hat{n}_j)^2} \right) \right]^{-\frac{1}{2}},$$
$$(4.5)$$

where

$$\lambda_i = (\sigma_{i\parallel}^2 - \sigma_{i\perp}^2)/(\sigma_{i\parallel}^2 + \sigma_{j\perp}^2), \lambda_j = (\sigma_{j\parallel}^2 - \sigma_{j\perp}^2)/(\sigma_{j\parallel}^2 + \sigma_{i\perp}^2). \qquad (4.6)$$

From this expression, one recovers the range parameters for two important special cases, namely: two identical spheroids ($\lambda_i = \lambda_j$) and the case in which one or both of the particles is a sphere ($\lambda_i = 0$ or $\lambda_i = \lambda_j = 0$). To match the hard-core nature of the interaction potential, we employ the simplification $\sigma_{ij} = \sqrt{2}\sigma(\hat{n}_i, \hat{n}_j, \hat{r}_{ij})$ since $\sqrt{2}(a^2 + b^2)^{1/2} = |a + b|$ when $a = b$. Hence, $\sigma_{ij} = 2\sigma_\perp$ (rather than $\sqrt{2}\sigma_\perp$) when two identical spheroids have their $\sigma_\perp$ axes heads on ($\hat{r}_{ij} \cdot \hat{n}_i = \hat{r}_{ij} \cdot \hat{n}_j = 0$), and likewise for the other cases. We note that the method used in this study to realize exactly the hard-core repulsion is through the determination of geometric overlapping conditions, which is well illustrated in Ref.[109].

We use standard Monte Carlo simulation in the NVT ensemble with periodic boundary conditions to investigate the encapsulation system. Notice that the system studied here is expected to locate in the micelles-rich gas phase regime, in which the main clustering mechanism is through monomer addition while cluster-cluster aggregation is suppressed. [105, 106, 107, 112] Hence, the conventional Metropolis Monte Carlo scheme employing local particle moves is sufficient. [116] Nevertheless, for the system with a much higher particle density where hierarchical self-assembly becomes important, a more sophisticated geometric cluster algorithm needs to be applied to increase the efficiency in sampling phase space. [117]

In the simulation, for simplicity, we choose $u_{ee} = u_{ss} = u_0$, where u_0 is the unit of energy. As is customary, we report quantities in terms of reduced units. We fix the number density of the spheroids to be $\rho_e = 0.04$, corresponding to the micelle gas regime of the phase diagram for the temperatures studied. [105, 112] Furthermore, we set $\sigma_\perp = 0.5$ and $\sigma_\parallel = 0.3$ ($\varepsilon = 0.6$) for the encapsulating spheroids. The simulation starts from a random initial monomer configuration. In each Monte Carlo step, a translation and then a rotation trial are tested given each particle's current position and orientation. The maximum step size for the trial in translation and rotation is set to be 0.02 and 0.04 for each direction and Euler angle, respectively. We track the equilibration of the system by monitoring the evolution of the potential

energy for a significant (typically $3 \times 10^6 - 10^7$) Monte Carlo steps (MCS). We determined that the system is at (or close to) equilibrium once the potential energy curves level off and converge to approximately the same lowest plateau starting from different initial configurations. Thus, the total simulation time varies from case to case. The results are then collected and, for good statistics, taken over at least ten runs inside the control groups.

4.3   Results and Discussion

In encapsulation systems, the encapsulation is carried out by the co-assembly of the agents and guests. The relationship of the interactions between the same types and different types of particles is rather important. Specifically, in the dilute system studied here, the agent spheroids are in the micelle gas phase and the guest spheres in the vapor phase if considered separately. [106, 118] Therefore, there are two more important mechanisms in the self-assembly process, namely, the encapsulation of the spheres by spheroids and the micellization of the spheroids themselves. In this section, we present our results, focusing on the impact of both internal and external factors on these two mechanisms and, hence, the overall self-assembly behavior. Since the parameter space is rather large for the system, we focus on only four important factors to highlight possible approaches to control encapsulation. To study the effect of environmental conditions, we first consider two major factors, namely the range of particle-particle interactions and the system temperature (or, equivalently, the interaction strength). We then consider the impact of guest particle size and affinity to the agent on encapsulation, respectively.

4.3.1   Effect of interaction range

The interaction range can be tuned in practice by modifying the physical conditions of the solvent if self-assembly occurs in solution. [106] In order to form isolated encapsulating clusters, controlling the confining shell and hence the behavior of the agents in the system is important. Therefore, we first examine a system comprising

only the encapsulating agents, namely Janus spheroids. We vary the well-width w of the pair potential, which changes the interaction range of the spheroids in the simulation. To study the role of w in determining cluster structure, we evaluate the distribution of the scalar product $\hat{n}_1 \cdot \hat{n}_2$ for all the pairs of bonded spheroidal particles at the end of the simulations. The results are presented in Fig. 4.1 A. We note that $\hat{n}_1 \cdot \hat{n}_2 \approx 1.0$ (-1.0) indicates that the patch orientation vectors of two particles are nearly parallel (antiparallel). From the figure, we find that there are two typical patterns for the distribution curves. For well widths in the range $0.2 \leq w \leq 0.4$ the curves are bimodal while, for $w = 0.5$, the peak height near -1.0 is diminished, possibly implying a difference in cluster structure.

In Figs. 4.1 B and C, we show examples of typical clusters from runs with $w = 0.2$ and $w = 0.5$, respectively. These two clusters are of similar size and are both well rounded. To obtain further information about these structures, we plot the distance distribution for member particles of a cluster from their center of mass in Fig. 4.1 D. As shown in the plot, for $w = 0.2$, the cluster is approximately a double-layer vesicle. The patches of its inner shell particles point outward to face the patches in the outer shell (hence the inner shell's surface is mostly red in color from Fig. 4.1 B), which is quite similar to a liposome. Furthermore, the average distances for two shells to the center of mass are 0.98 ± 0.03 and 1.57 ± 0.10, respectively. Since $\sigma_\parallel = 0.3$, this implies that the inner space of the first shell has a radius about 0.68, and that the two shells are barely touching as their separation is about $2\sigma_\parallel$.

By contrast, for the cluster having $w = 0.5$, the distribution of particles around its center of mass reveals that the cluster has a loose structure, and hence is rather 'liquid-like'. This is because, for large w, the attraction becomes sufficiently long-ranged so that there are more degenerate configurations with the same potential energy for the cluster. Thus, the particles need not remain in close proximity inside the cluster and thereby gain additional entropy. Consequently, there is enough space for cluster reorganization, with the result that there are more interacting pairs. Therefore, the number of face-to-face patch pairs is reduced for $w = 0.5$, leading to a reduction of the peak height close to $\hat{n}_1 \cdot \hat{n}_2 = -1.0$ in the orientational distribution curve. Thus, one can roughly classify the interaction range into two categories for
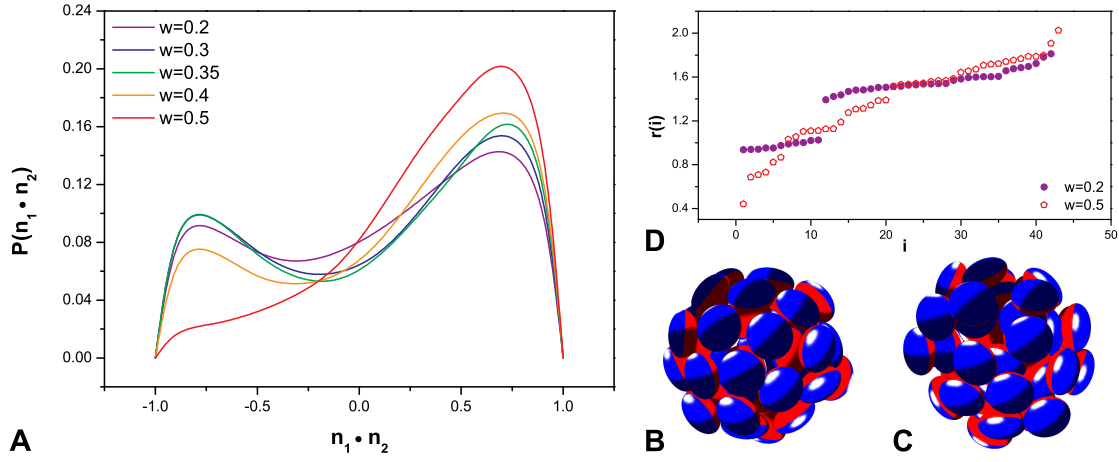
Figure 4.1: (A) Probability distribution of orientational correlation $(\hat{n}_1 \cdot \hat{n}_2)$ for all pairs of bonded Janus spheroidal particles having aspect ratio $\varepsilon = 0.6$ for different interaction ranges. (B) A typical cluster of 42 particles for a system having a well-width $w = 0.2$. (C) A typical cluster of 43 particles for a system having a well-width $w = 0.5$. The attractive hemi-surface patches are colored in red. (D) A summary of particle distances from a cluster's center of mass, $r(i)$, for each particle i for the two clusters shown in (B) and (C).

Janus spheroids, namely short-ranged ($w < 0.5$) and long-ranged ($w \geq 0.5$).

Previous investigations were done for $w = 0.5$. [113] Here, without loss of generality, we fix the well-width to be $w = 0.35$, which has the typical distinctive peaks for the short-range interaction regime, for the remaining simulations in this study. Note that w also controls the range of agent-guest and guest-guest interactions in the encapsulation system. We find that such a change in well-width does not have a significant impact on the system's self-assembly and encapsulation behavior. More importantly, considering the encapsulation efficiency of spheroids, the associated monodisperse encapsulation in which each sphere is entrapped by a single-layer of Janus spheroids is desirable. Hence, the ability to form more regular shells also makes the short-range interaction favorable for this purpose.
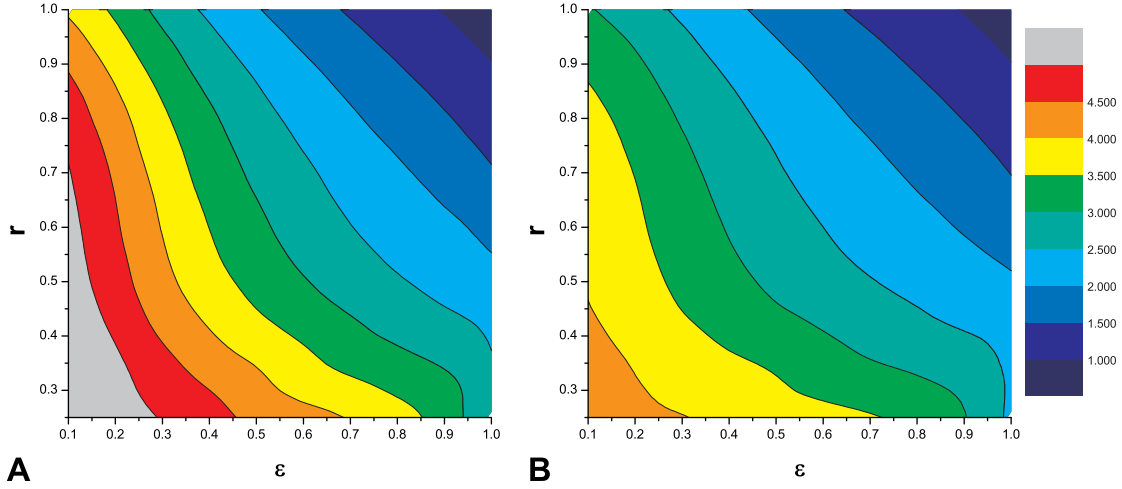
Figure 4.2: A density map showing the ratio of virial coefficients, $(B_2^*)_{es}/(B_2^*)_{ee}$, for the encapsulating spheroids as a function of aspect ratio ε and encapsulated sphere radius r for (A) $T = 0.33$, and (B) $T = 0.25$, respectively. The well-width w is fixed at 0.35.

4.3.2 Effect of system temperature

We use the second virial coefficient B_2, a measure of the effective interaction strength between particles, to study the effect of temperature on the encapsulation system. [119] By definition,

$$B_2 = -\frac{1}{2V} \int d\vec{r}_i \int d\vec{r}_j \left[e^{-\beta U(r_{ij})} - 1 \right]. \tag{4.7}$$

Here, we employ a reduced B_2, i.e. $B_2^* \equiv B_2/B_2^{hc}$ in the discussion, where B_2^{hc} is the hard-core second virial coefficient. For the encapsulation system, we focus on two types of interactions, the agent-guest (es) interaction and the agent-agent (ee) interaction, for which the corresponding strengths are set as $u_{es} = u_{ee} = 1.0$. We calculate B_2 via numerical integration of Eq. (4.7) and plot the ratio $(B_2^*)_{es}/(B_2^*)_{ee}$ as a function of the spheroid aspect ratio ε and sphere radius r at temperatures $T = 0.33$ and $T = 0.25$. The results are shown in Figs. 4.2.

From the figures, we find that the trend in the variation of the ratio is similar for both temperatures (i.e., the value decreases from the lower left corner to the upper

right corner). It is also evident that $(B_2^*)_{es}/(B_2^*)_{ee}$ tends to be larger (although the magnitudes of $(B_2^*)_{es}$ and $(B_2^*)_{ee}$ both decrease) at higher temperatures for a given point in the $r - \varepsilon$ parameter space. These results indicate that the agent-guest bonding resulting in encapsulation decays more slowly than the agent-agent bonding with increasing temperature (over a reasonable range). Therefore, as the temperature goes up, the disintegration of agent shells becomes easier compared to the dismissal of encapsulation structures. Alternatively, at a higher temperature, the encapsulation mechanism is enhanced relative to the micellization of spheroids in the system.

This behavior suggests that, for the system in which a further increase in the degree of encapsulation leads to a decrease in free energy, an optimization strategy employing thermal annealing may be useful to increase the number of agent-guest bonds and, hence, to promote encapsulation. In reality, a self-assembling system may become kinetically trapped in some (long-lasting) metastable states (i.e., local free energy minima on the free energy landscape) where the degree of encapsulation is low. Thus, thermal annealing (including heating and cooling treatments) can potentially provide the necessary impetus to escape from such local minima, thereby facilitating system equilibration. In summary, in view of the previous findings concerning the effect of the interaction range, we expect that the encapsulation structures formed by Janus spheroids and spheres are quite adaptive to the external environment factors, such as solution condition, temperature, etc.

4.3.3 Effect of guest size

Given some understanding of the adaptation of the encapsulation system to environmental conditions, consider next the encapsulation properties of the Janus spheroids. More specifically, we wish to examine how the agent spheroids act upon guest spheres having different sizes and different affinities with the agent. Recalling the vesicle structure in Fig. 4.1 B, the effective radius of the enclosed space is about 0.68 (for $w = 0.2$). Thus, one would expect that the 'cage' formed by spheroids could contain an object whose radius is less than 0.68. However, what happens if

the radius of the object exceeds 0.68? Would the spheroidal shell still contain the guest, perhaps by altering the packing of spheroids in the shell or by absorbing more spheroids to form a bigger shell?

To study the guest size effect, we vary the radius of sphere r from 0.1 to 1.0 for the guest particles in a system with $T = 0.25$ and number ratio $\alpha = 16$. Some typical equilibrium morphologies are shown in Fig. 4.3. Interestingly, we find that for increasing sphere size, encapsulation becomes less complete and, in particular, the encapsulation efficiency decreases dramatically as r increases. It can be seen from the figures that for $r = 0.3$, 0.4, and 0.5 (Figs. 4.3 A, B and C), the spheres are 100% encapsulated, while at $r = 1.0$ (Fig. 4.3 F) none of the spheres is fully covered (0% encapsulated).

One might conjecture that the low degree of encapsulation for large spheres is due to the lack of spheroids, since the total surface area of the spheres increases as the radius grows ($\propto r^2$) while there are not enough spheroids to cover it. To investigate this possibility, we constructed a control group having more spheroids than spheres ($\alpha = 60$). Typical morphologies for $r = 0.8$, 0.9, and 1.0 are shown in Fig. 4.4. As is evident from Fig. 4.4 A, the increase in α does affect the encapsulation. However, the encapsulation efficiency still decreases dramatically as the size of the encapsulated guest increases. Specifically, the degree of encapsulation is 50% for $r = 0.8$ in Fig. 4.4 A, and still 0% for $r = 1.0$ (Fig. 4.4 C), as before (i.e., for the case in which $\alpha = 16$). Moreover, for $r = 1.0$, rather than capturing the spheres fully inside, the spheroids form clusters by themselves and then attach to the spheres. Such behavior does not change even when adding more spheroids to the system.

These results suggest that as the guest size increases, the encapsulation mechanism is suppressed such that the micellization of the spheroids becomes dominant. Recalling the results shown in Figs. 4.2, one can find a hint for this trend. Specifically, for $\varepsilon = 0.6$, the ratio of $(B_2^*)_{es}/(B_2^*)_{ee}$ decreases as r increases. This indicates that, due to an enthalpic effect, the system has two regimes associated with the guest particle size r, namely, an encapsulation regime at small r and a micellization regime at large r. Also, there is an intermediate region in which the encapsulation
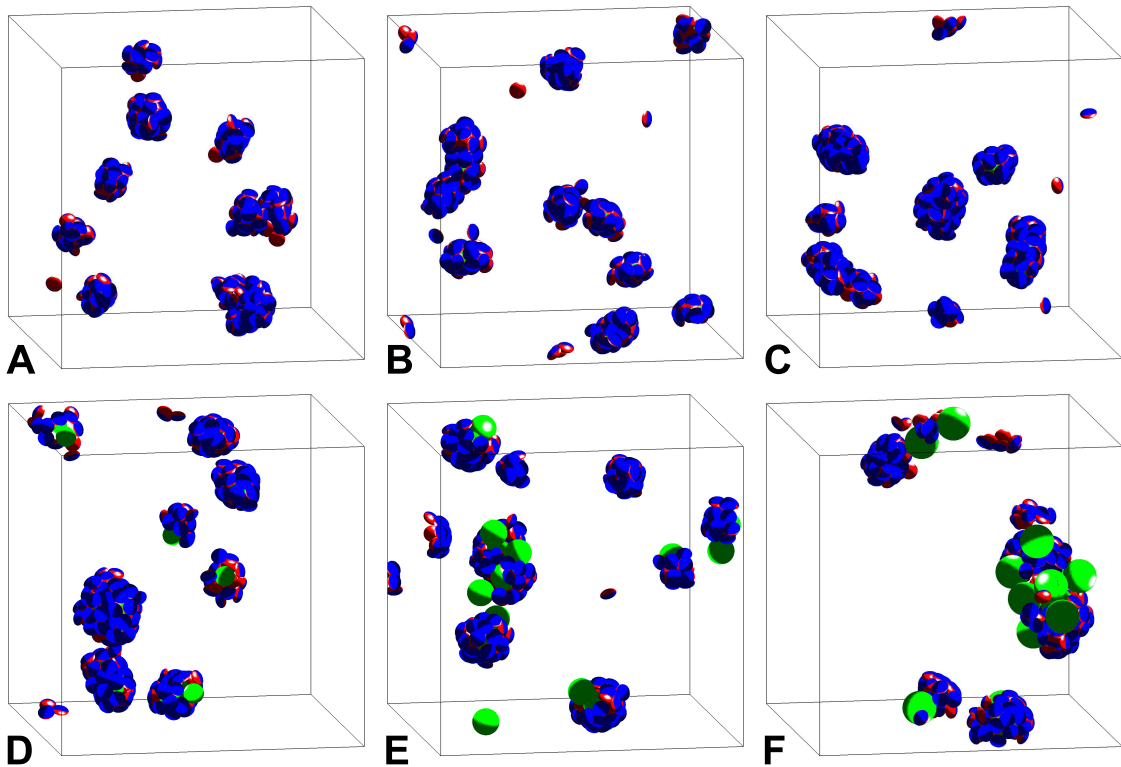
Figure 4.3: Typical configurations of the system ($\rho_e = 0.04$, $\alpha = 16$) with different encapsulated guest sizes, r, at $T = 0.25$. (A) $r = 0.3$, (B) $r = 0.4$, (C) $r = 0.5$, (D) $r = 0.6$, (E) $r = 0.8$ and (F) $r = 1.0$.

becomes frustrated as the micellization mechanism is competitive. Thus, one would expect a reduction in encapsulation efficiency inside the intermediate region.

Moreover, from the clustering behavior of Janus particles in the gas-phase regime, one finds some dominant peaks in the cluster size distribution. [105, 112] For example, for Janus spheres, the most frequent clusters are micelles of size 10 and vesicles of size 40. [105, 106] This implies that Janus particles have preferred curvatures for packing. Furthermore, such curvatures dictate the inner cavity sizes of the shell structures. Therefore, for guest sizes greater than the cavity size, there is an attendant distortion that alters the free energy of the shell. Thus, if the decrease in
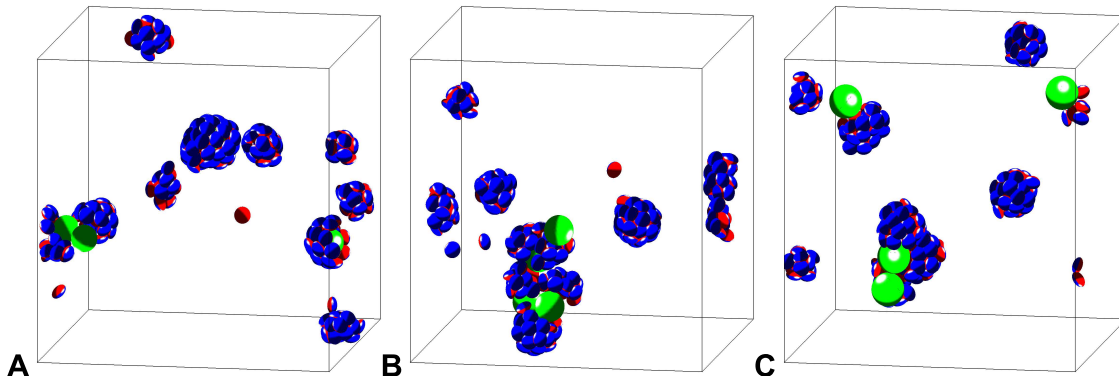
Figure 4.4: Typical configurations of the system ($\rho_e = 0.04$, $\alpha = 60$) with different encapsulated guest sizes, r, at $T = 0.25$. (A) $r = 0.8$, (B) $r = 0.9$, (C) $r = 1.0$.

potential energy associated with insertion of the guest does not compensate this difference in free energies, the preferred configuration is not encapsulation. Hence, with regard to the questions posed above, a cage formed spontaneously by the spheroids might be unable to accommodate oversized guests.

In assessing the potential for encapsulation, one must also consider entropic effects. For very small guest particles (such as $r \leq 0.1$), confinement is not preferred as particles can lower the free energy of the system via the increase in entropy associated with sampling more of configuration space. Indeed, this reduction may offset, or even exceed, the change in potential energy associated with binding with agents, with the result that the encapsulation efficiency for this system with small guest particles is less than that for intermediate size guest particles. As a consequence, the encapsulation by Janus spheroids has a size selectivity range (having both an upper bound and a lower bound) based on the diameter of guest particles.

More specifically, one can identify several regimes that are dominated by entropic effects, encapsulation, frustrated encapsulation, micellization and guest particle size. From Fig. 4.4, one would expect that the densities (activities) of agents and guests may shift the boundaries between those regions. Nevertheless, the trend remains the same. In general, the agents cannot encapsulate excessively large or small particles.

Also, the encapsulation efficiency decreases in the frustrated encapsulation regime. This conclusion pertains to the case in which the interaction strengths between agents and guests are equal ($u_{es} = u_{ee} = 1.0$). In the next section, we assess the impact of the agent-guest interaction.

4.3.4   Effect of agent-guest interaction strength

Next, we study the impact of the spheroid-sphere interaction strength, u_{es}, on the encapsulation behavior. For this purpose, we sweep the parameter space of u_{es} for different guest sizes, focusing specifically on the regime in which u_{es} is not excessively large. In Fig. 4.5, we show typical system configurations for two guest sizes, $r = 0.4$ and $r = 0.6$, for three interaction strengths, $u_{es} = 0.5$, 1.5 and 2.0, respectively. From these results, we expect that, for particles with $u_{es}/u_{ee} \ll 1.0$ (cf. Figs. 4.5 A and D), encapsulation is frustrated regardless of sphere size. Instead, spheroids and spheres form separate clusters. On the other hand, for $u_{es}/u_{ee} > 1.0$, encapsulation is promoted (Fig. 4.5 E and Fig. 4.3 D); however, this promotion is not so significant as to negate the guest size effect (as one can see from Figs. 4.5 E and F) in the range of interaction strength we consider here.

Moreover, from a comparison of Figs. 4.5 B and C, it is evident that monodisperse encapsulation can be facilitated by increasing u_{es}, but for an appropriate guest size. This is also understandable, as a large u_{es} facilitates the completion of the encapsulation shell and a complete shell shields both guest particle and shell agents from other particles. Nevertheless, for larger guests, the increase in u_{es} may result in large cluster aggregates, since the frustration of encapsulation due to the size effect leads to open structures that still attract each other (Figs. 4.5 E and F). From these results we conclude that, in addition to guest-size selection, there is also a selectivity associated with the interaction strength (i.e., guests that have comparable or stronger interaction with the agents can be encapsulated). Moreover, monodisperse encapsulation is also achievable for this system. However, further investigation of the parameter space is necessary to identify a regime for optimal encapsulation.

Finally, we conclude this section with some additional remarks about the particle
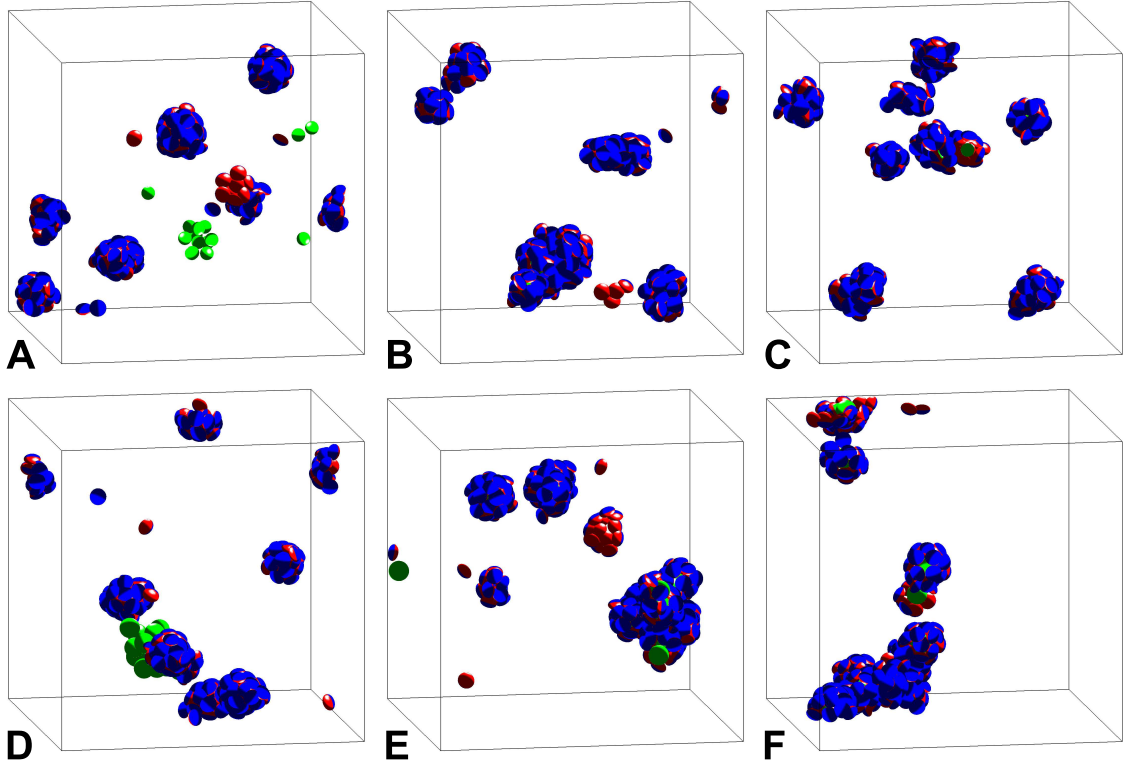
Figure 4.5: Typical configurations of the system ($\rho_e = 0.04$, $\alpha = 16$) having different agent-guest interaction strengths u_{es} at temperature $T = 0.25$. The upper panel is for the guest size $r = 0.4$ at (A) $u_{es} = 0.5$, (B) $u_{es} = 1.5$ and (C) $u_{es} = 2.0$, and the lower panel is for the guest size $r = 0.6$ at (D) $u_{es} = 0.5$, (E) $u_{es} = 1.5$ and (F) $u_{es} = 2.0$, respectively.

interaction by considering two types of realistic systems. First, for the case in which the attraction inside the encapsulation system is mediated by depletion force, one finds, based on the Derjaguin approximation (assuming the system is in the colloid-limit regime), that the interaction strength is proportional to $R_{eff} = R_1 R_2/(R_1 + R_2)$, where R_1 and R_2 are the radii of curvature of the interacting objects at the point of closest approach. [120] As an estimate, for a spheroid in the interaction heads-on (i.e., patch orientations align along the center-to-center direction), $R_1 = \sigma_\perp^2/\sigma_\parallel = 0.5^2/0.3 \approx 0.83$ and $R_2 = r$ for a sphere. Thus, the ratio of the spheroid-sphere and

spheroid-spheroid interaction strengths in this scenario is $2r/(r + R_1)$, and hence varies from 0.22 to 1.09 for $r = 0.1$ to $r = 1.0$, respectively. Also, a ratio of 2.0 (the largest ratio we consider in the case study) is physically unachievable. Thus, one would expect that the selectivity of encapsulation in this system is significant, and that the window for encapsulation depends critically on both size selectivity and interaction strength.

For other cases in which the interaction between spheroid and sphere is much stronger than that between spheroids (i.e., the ratio is $\gg 1.0$), the spheroid is tightly trapped by the sphere via the short-range attraction (large adsorption free energy). Hence, the upper boundary of the guest size for encapsulation-dominant regime is significantly raised and the guest size effect may even be overcome. Thus, as one might expect, full adsorption/encapsulation can result regardless of the guest's size and shape. This is similar to the case of (Pickering) emulsion systems where amphiphilic Janus particles functioning as stabilizers are absorbed at liquid-liquid interfaces. [121, 122] Nevertheless, one should note that this interfacial behavior of Janus particles and the selective encapsulation properties presented in this study apply in different regimes of interaction strength.

4.4 Conclusions

In summary, we have studied several properties of the encapsulation of guest particles by Janus oblate spheroids in a dilute system using Monte Carlo simulation. We find that, in general, encapsulation is quite adaptive to variations of the environmental conditions via changes in the particle interaction range as well as the system temperature. For both long-range and short-range interactions, the encapsulation of the isotropic spheres by the Janus spheroids can be quite effective. Based on the investigation of the temperature effect, we find that agent-guest bonding dominates agent-agent bonding with increasing temperature and, hence, an annealing strategy may optimize the encapsulation process (which is thermodynamically favorable). Moreover, by a systematic exploration of the parameter space of the guest size and

the interaction strength, we observe two kinds of encapsulation selectivity given a sufficient number of agents, suggesting that the Janus oblate spheroid agent has a particular preference for the guest particles.

We have shown that, for a reasonable range of interaction strength (comparable to the agent-agent interaction), an agent does not trap small or large particles, leading to a low encapsulation efficiency. These findings highlight the collective behavior of the agents, indicating that the agents are quite locked in when spontaneously forming shells. As a result, such shell structures are especially robust as there is a size selectivity associated with encapsulation. The agent activity only slightly affects this selectivity, and modest changes in the agent-guest interaction do not help in overcoming the guest size effect.

We note that the mathematical model and simulation methods presented here are quite transferrable in general, and may therefore be extended to study other systems with different types of particles and inter-particle interactions, etc. From these considerations, we speculate that the nature of selective encapsulation may not be unique to Janus spheroids, but may be quite general for other types of Janus particles as well as patchy particles. Therefore, particles that form dispersed capsules (micelles/vesicles) from self assembly could potentially be used as encapsulating agents as well. Furthermore, assuming that in the system the agent-guest interaction is not "overwhelmingly" stronger than the agent-agent interaction, selective encapsulation may also be possible. The substantiation of these conjectures, however, requires additional studies.

Finally, from a previous investigation, we have noted the correspondence between Janus prolate spheroids and amphiphilic lipid molecules. [111] Thus, another important encapsulation process performed by lipids can possibly be translated to a system of colloidal particles in which the length scale is different. Thus, encapsulation by Janus prolate spheroids may be an interesting subject for future work. However, such studies may require a more sophisticated potential model, such as one with an angle-dependent strength. [123] In summary, we believe that simulations can provide beneficial insight into practical encapsulation strategies, and selective encapsulation is a promising avenue for many practical applications.

Another situation which we believe that simulations can provide insight is adsorption of molecules onto substrate. Simple models of the adsorption of molecules can qualitatively predict many kinds of phase behavior including critical temperature, phase diagrams, and even structures formed in said phases. Chapter 5 studies a model of the adsorption of C_3 symmetric, Y-shaped molecules on a hexagonal lattice with and without patterned lattice binding sites. We determine the phase diagram of said system without lattice binding interaction, and determine the effect of patterned lattice binding sites on the critical temperature of the system.

Chapter 5

Phase Transition in a Lattice Model of Y-Shaped Molecules

5.1 Introduction

Molecules adsorbed on solid substrates often self-organize into highly ordered states. Of particular interest are networks formed by C_3 symmetric, "Y"-shaped organic functional molecules (tripods) at solid/liquid interfaces. This is due to their ability to form networks of regularly spaced nanometer-sized pores. Simulational, and experimental work has shown that the networks formed by the adsorbed molecules is largely dependent on the size of the arms of the molecule.

Szabelski *et al.*[124] explore a model of tripods on a two-dimensional, hexagonal lattice. The tripods are rigid molecules consisting of a center, and three arms, each of which consist of n beads. The center, and each bead occupy one lattice site, and interact with nearest neighbor beads of separate molecules through a binding energy of strength ϵ. Substrate binding interactions are ignored. Szabelski *et al.* explore arms of length $n = 1, 2, 3, 4, 5$, and find for $n > 1$, three phases could be present. Two phases consist of regularly spaced porous structures with different pore size and shape, and the third is the typical lattice gas. The tripods of arm length $n = 1$ only formed a dense phase with no pores, and a lattice gas. It is the case of $n = 1$ that

we explore in this paper, along with changes in bead, and substrate interactions. The effect of different types of substrate binding has been explored through both simulation and experiment. Rzysko and Borowko simulated heterogenous dimers and investigated the effect of substrate interactions on the critical temperature of the system[125]. Substrates consisted of 50% coverage of attractive sites. The substrates were formed by alternating rows of width w of attractive sites with binding strength of ϵ_{sub}, and rows of width w consisting of sites that had no binding interaction. Substrate binding strengths of $\epsilon_{sub} = \frac{\epsilon}{4}$ and $\frac{\epsilon}{2}$ were chosen, where ϵ was the magnitude of the bead interactions. Row width w ranged from 1 to 5. It was observed that the critical temperature of the system decreased with increasing row width w as well as binding strength ϵ_{sub}.

The work we present explores the critical temperature, and changes in the phase diagram of the $n = 1$ tripod due to changes in bead interactions; Namely, we ignore any interactions of the center with other beads. We calculate the critical temperature employing grand-canonical Monte Carlo simulations along with the usual histogram reweighting and multicanonical biasing methods. We also propose to execute these methods, adding substrate binding interactions to beads similar to those used by Rzysko and Borkowitz, and determine the effect the binding interaction strength, as well as strip width play on the critical temperature of the system in a future publication. The outline of our paper is as follows: In Section II we define our model and the method by which we study it. In Section III we present our results, namely that this model belongs to the Ising universality class. This particular result was expected *a priori* since the order parameter is a scalar. Using finite-size scaling (FSS) methods, we also obtain the liquid-liquid phase separation curve of the tripod. We provide results for the finite-size system critical point, using a standard scaling analysis. In Section IV we present a brief conclusion.
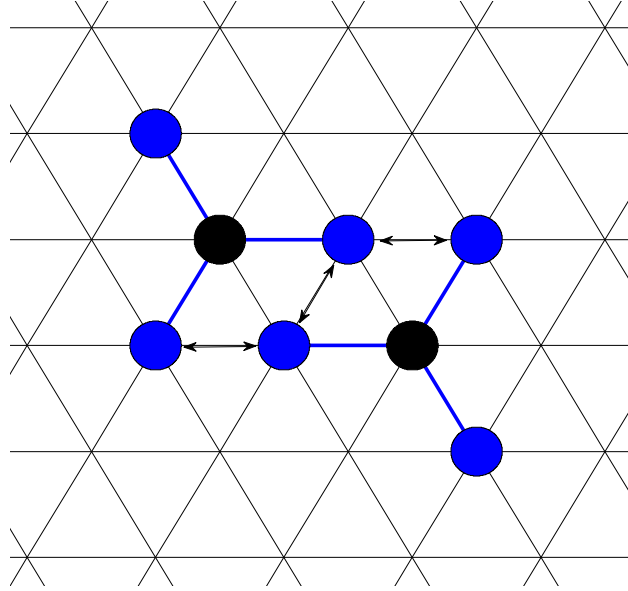
Figure 5.1: Each center (black circle) and arm (blue circle) occupy one lattice site, and each arm is physically bonded to the center(blue line). The interactions between arms and their nearest neighbors are denoted by $\longleftrightarrow$.

5.2 Model and Simulation

Our model of the Y-shaped molecule is implemented within the environment of a two-dimensional hexagonal lattice with side length L containing L^2 sites. Periodic boundary conditions are employed. Each of the N molecules occupies 4 lattice sites; the four include one central site and 3 rigid *distal* arms. This leads to a maximum number density of the system ρ of 0.25. The interactions included in this study are those between distal arms, and their respective nearest-neighbor distal arms, as shown in Fig.5.1, each with interaction strength of J. For simplicity, there are no center-to-center, center-to-distal arm, or any lattice binding energies. The total energy of the system U is then the summation of all distal arm-distal arm interactions. We execute grand-canonical Monte Carlo (GCMC) simulations. To analyze the data and obtain the phase diagram, we use the Bruce-Wilding finite-size scaling (FSS) techniques[126, 127], along with histogram reweighting and multicanonical sampling methods[128], to compile the phase diagram of this system. The fact that

60

the order parameter for this model (defined below) is a scalar suggests that this Y-molecule model belongs to the Ising universality class, as we show in Section III.

Assuming that our model belongs to the Ising universality class, the critical point of our system can be determined by matching the probability density function (PDF) of the ordering operator M of our system with the universal distribution of the two-dimensional Ising class. The order parameter M for the fluid is given by[126, 127]

$$M = \frac{1}{1 - sr}[\rho - su], \tag{5.1}$$

where $u = U/N$ is the energy density, and s and r are system specific parameters to be determined later. Similar to the order parameter M, the energy-like parameter $\mathcal{E}$ is given by

$$\mathcal{E} = \frac{1}{1 - sr}[u - r\rho]. \tag{5.2}$$

The Ising universality class has two relevant scaling fields, namely h, the ordering scaling field, and τ, the thermal scaling field. For fluids in this universality class, τ and h are defined as

$$\tau = \omega_c - \omega + s(\mu - \mu_c), h = \mu - \mu_c + r(\omega_c - \omega), \tag{5.3}$$

where $\omega = J/kT$, μ is the reduced chemical potential in units of kT, and the subscript c denotes the critical point. The parameters r and s determine the degree of mixing in the relative scaling fields as well as M and $\mathcal{E}$.

During a simulation in a system size of side L, at fixed values of μ and ω, we record the molecule number density ρ and the energy density u, from which we determine the joint probability density function $P(\rho, u)$. The joint PDF, $P(M, \mathcal{E})$, for the rescaled variables, M and $\mathcal{E}$, is related to the joint distribution of density and energy such that $P(M, \mathcal{E}) = (1 - sr)P(\rho, u)$. We focus mostly on the order parameter PDF $P(M) = \int d\mathcal{E} P(M, \mathcal{E})$. At the critical point, all members of the Ising universality class have the same fixed point distribution function. In the simulations, this fixed point distribution and the PDF of our model are expressed as $\tilde{P}_M(x)$ and $P_L(M)$ respectively, where $x = \alpha_M^{-1} L^{\beta/\nu}(M - M_c)$. $\beta = 1/8$ and $\nu = 1$ are the critical exponents of the order parameter and correlation length of

the two-dimensional Ising class, respectively. α_M^{-1} is a scaling parameter such that $\tilde{P}_M(x)$ has unit variance. Therefore, the PDF $P_L(x)$ of our model must also match $\tilde{P}_M(x)$ at the fixed point. It is only for large L that the numerically obtained PDF tends to the fixed point distribution $\tilde{P}_M(x)$.

The fixed point function $\tilde{P}_M(x)$ for the two-dimensional Ising model has been determined from previous work [126]. For one system size, by varying T, μ, and s, and matching the numerically obtained $P_L(x)$ with $\tilde{P}_M(x)$, we can determine the $T_c(L)$, $\mu_c(L)$, and $\rho_c(L)$ of our model at said system size. By repeating this process for multiple system sizes, the bulk critical temperature(T_c), chemical potential(μ_c), and density(ρ_c) can be extrapolated. We obtain the parameter r from the slope of the μ-ω coexistence line at criticality[127] as seen in Fig.5.2.

To avoid performing numerous simulations, we use the standard method of histogram reweighting. To analyze the data and obtain the phase diagram, we use the Bruce-Wilding FSS techniques outlined here[126, 127, 129, 130]. In order to obtain the critical parameters of the infinite system, we performed GCMC simulations for systems with side lengths 30, 40, 50, and 60 with periodic boundary conditions. The observables recorded during the simulation were u and ρ, from which, $P(\rho, u)$, $P(\rho)$, $P(M, \varepsilon)$, and others were calculated. For each temperature, chemical potential, and system size, the simulation ran for 5,000 - 6,000 Monte Carlo steps (MCS), and for 15,000 - 25,000 Monte Carlo steps for simulations implementing and not implementing biasing techniques respectively, before recording the density and energy of the system. Each MCS comprises N attempts to change the system either by a molecule translation, rotation, insertion, or removal. The changes that the GCMC attempts to make to the system are defined as follows:

Translation Attempt to move the center of a randomly selected molecule to one of the 6 nearest neighboring sites of the center.

Rotation Attempt to rotate a randomly selected molecule either clockwise, or counter-clockwise about the molecule center.

Insertion Attempt to place a molecule, with a random orientation, on a randomly

chosen lattice site.

Removal Attempt to remove a randomly selected molecule.

This algorithm is ergodic. The density and energy of the system are recorded a total of 150,000 - 250,000 times over the length of the simulation, with 1,000 - 2,000 and 2,000 - 4,000 MCS in between each recording for systems with and without the preweighting function, respectively.

5.3   Results

The method we use to find the bulk critical parameters is as follows. First, we plot $P_L(x)$ for varying system sizes and find best fits to the universal fixed point $\tilde{P}_M(x)$ by varying $T_c(L)$, $\mu_c(L)$, and s. A sample best fit of $P_L(x)$ to this fixed point is shown in Fig.5.3 and shows that, within the accuracy of our study, our model belongs to the Ising universality class. Next, we use the FSS predictions[129] that

$$T_c - T_c(L) \propto L^{-(\theta+1)/\nu} \tag{5.4}$$

and

$$\mu_c - \mu_c(L) \propto L^{-(\theta+1)/\nu} \tag{5.5}$$

to determine the bulk values of the critical temperature and critical chemical potential. In these equations, T_c and μ_c are the actual bulk critical temperature and chemical potential, and $T_c(L)$ and $\mu_c(L)$ are the apparent bulk critical temperature and chemical potential determined from matching $P_L(x)$ to the fixed universal distribution $\tilde{P}_M(x)$. θ is a correction to scaling exponent. We use the value $\theta = 1.35$, as calculated by Barma and Fisher[131], which coincides with the conjecture of Nienhuis[132] for the two-dimensional Ising system. The next step is to record $T_c(L)$ and $\mu_c(L)$ for each system size, plot $T_c(L)$ and $\mu_c(L)$ versus $L^{-(\theta+1)/\nu}$, and then extrapolate to the infinite system size for both $T_c(L)$ and $\mu_c(L)$. We then record the extrapolated points as T_c and μ_c. The resulting graphs of $T_c(L)$ and $\mu_c(L)$ versus $L^{-(\theta+1)/\nu}$ are given in Fig.5.4.
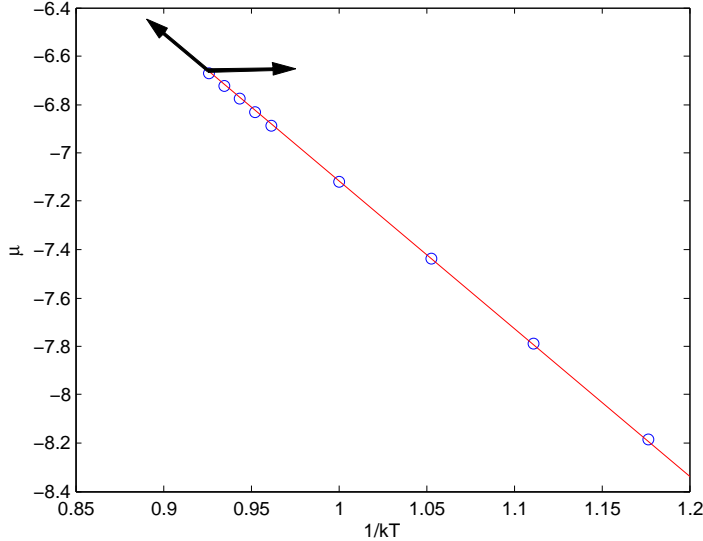
Figure 5.2: Plot of reduced chemical potential μ versus the reduced interaction strength ω. The parameter r is the slope of this curve at the critical temperature and is found to be $r = -6.111$.

FSS also predicts a similar correction to the critical density of the model, namely

$$\rho_c - \rho_c(L) \propto L^{-(d-1/\nu)}, \tag{5.6}$$

where ρ_c is the bulk critical density, $\rho_c(L)$ is the apparent critical density of a system of size L at T_c and μ_c, and $d = 2$ is the dimensionality of the system. Similar to the cases of T_c and μ_c, ρ_c is extrapolated from the plot in Fig.5.5 and is $\rho_c = 0.127\pm0.002$.

The coexistence curve was determined through a series of GCMC simulations at varying temperatures below the critical region, implementing the histogram reweighting and multicanonical sampling techniques discussed previously. Coexistence between two phases at a temperature T is confirmed when the areas underneath the two peaks in the density distribution $P(\rho)$ are equal. The peak densities are recorded and plotted on the phase diagram. Examples of some density distributions for varying T at coexistence are shown in Fig.5.6.

In temperature regions apart from the critical region, finite-size effects are expected to be negligible since the correlation length is much smaller than that of the
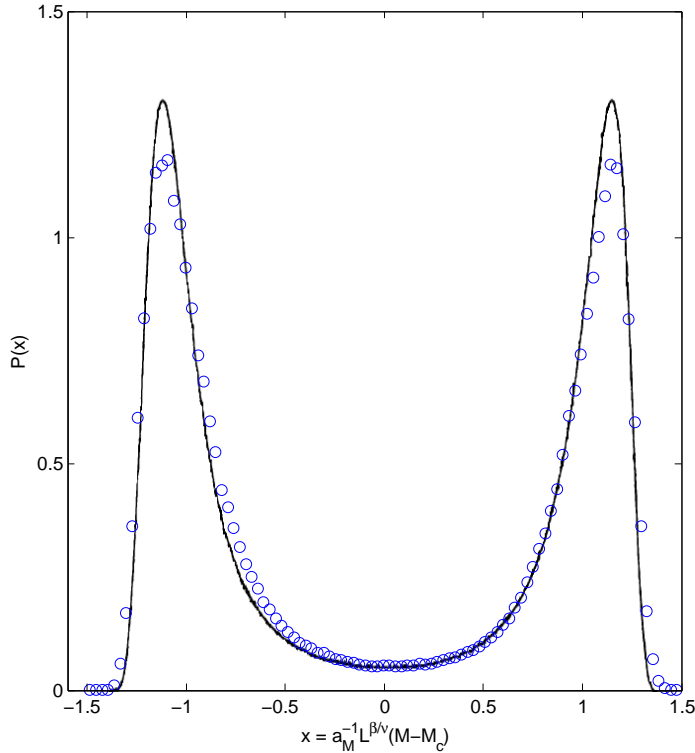
Figure 5.3: $P_L(x)$ (blue circle) for $L = 60$ and the universal fixed point distribution $\tilde{P}_M(x)(-)$ versus x. $T_c(L)$ and $\mu_c(L)$ were $T_c(L) = 1.084$ and $\mu_c(L) = -6.477$. Reproduced by permission of IOP Publishing, N. B. Wilding, and A. D. Bruce, "Density fluctuations and field mixing in the critical fluid" Phy.: Condens Matter **4**, 3087-3108 (1992). Copyright 1992 by IOP Publishing. All rights reserved[127].

size of the system. With this expectation, the density peaks of $P(\rho)$ found in our finite systems at different temperatures below the critical region will still mimic that of an infinitely large system. A phase diagram of the infinite system is constructed by determining the positions of the peaks in $P(\rho)$ for sub-critical temperatures. As an additional check on this estimate of the equilibrium densities, we also calculate the average density of each the two phases present by using the PDFs to calculate these statistical averages. Our results are shown in Fig.5.7, where the FSS estimates

(a) Apparent $T_c(L)$ vs $L^{-(\theta+1)/\nu}$

(b) Apparent $\mu_c(L)$ vs $L^{-(\theta+1)/\nu}$
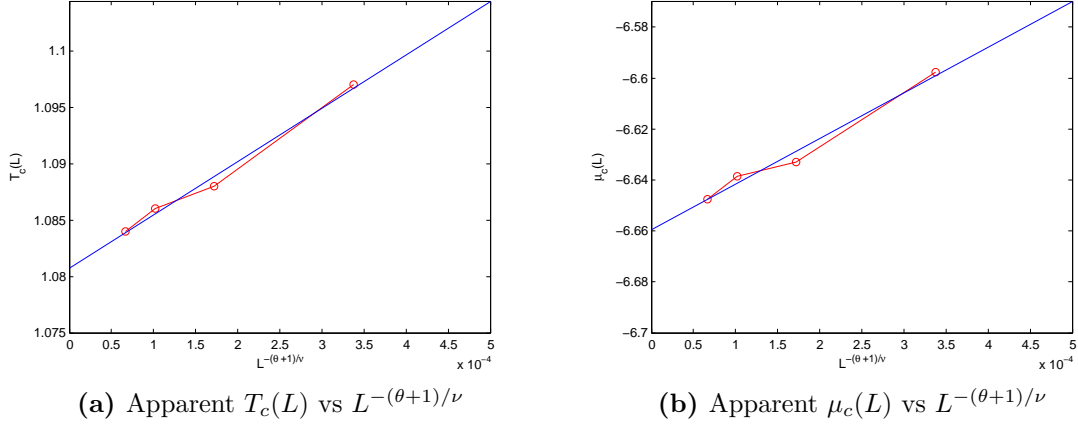
Figure 5.4: a.) Plot of apparent bulk critical temperature determined from matching $P_L(x)$ to $\tilde{P}_M(x)$. b.) Plot of the apparent bulk critical chemical potential determined from matching $P_L(x)$ to $\tilde{P}_M(x)$. The extrapolated critical temperature and chemical potential are $T_c = 1.081{\pm}0.002$ and $\mu_c = -6.66{\pm}0.01$.
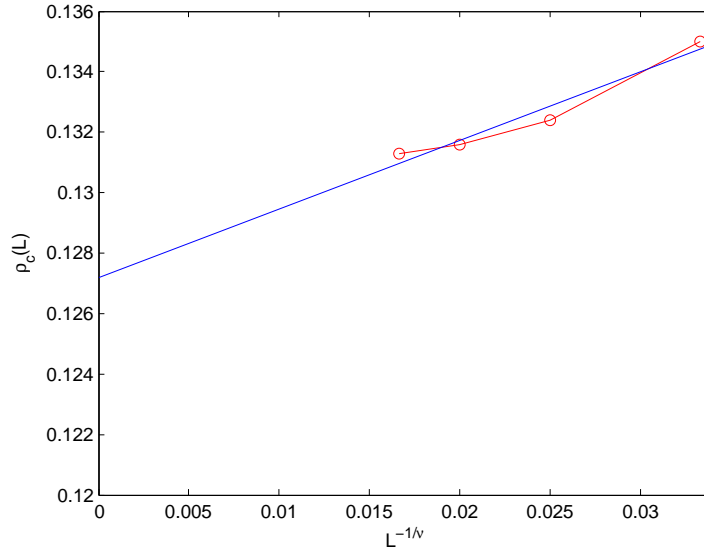
Figure 5.5: Plot of the apparent $\rho_c(L)$ vs $L^{-1/\nu}$. The extrapolated $\rho_c = 0.127 \pm 0.002$.
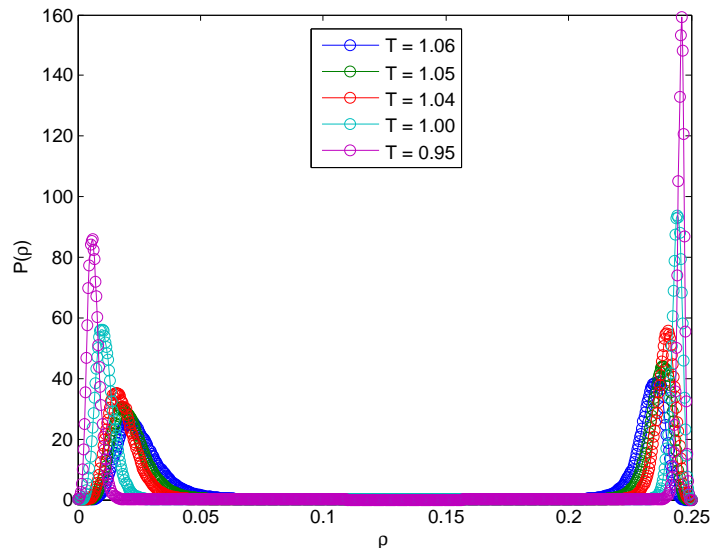
Figure 5.6: Plot of estimated $P(\rho)$ versus ρ for varying temperatures at coexistence. All $P(\rho)$ were determined as described in the text.

r	s	T_c	μ_c	ρ_c
-6.111	$\simeq 0.05$	1.081 ± 0.002	-6.66 ± 0.01	0.127 ± 0.002

Table 5.1: List of all critical point parameters

of T_c and ρ_c are also plotted.

We fit the points of our phase diagram to a power law of the form[129]

$$\rho \pm \rho_c = a|T - T_c| \pm b|T - T_c|^\beta. \tag{5.7}$$

This fit is also included in Fig.5.7. There is a small asymmetry evident on the high density side of the phase diagram, but not as pronounced as the one found experimentally or numerically in 3D for IgG. We show the critical parameters determined through the FSS method in Table 5.1. We also show in Fig.5.8 a typical configuration of a high density system in equilibrium.
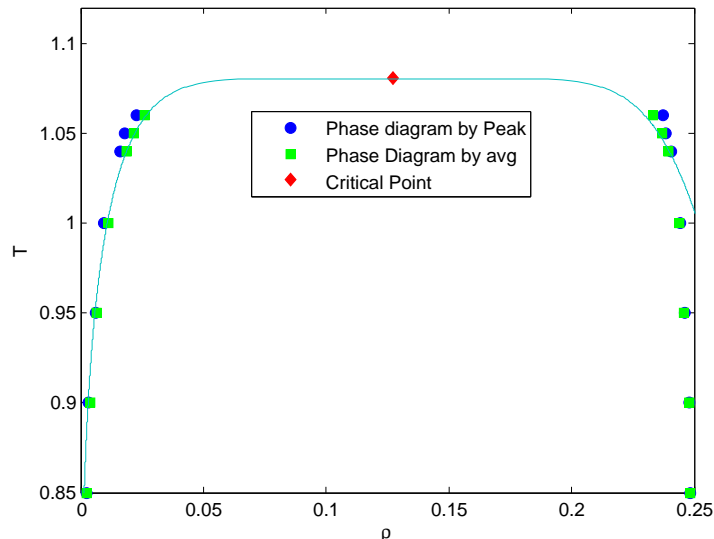
Figure 5.7: The reduced temperature versus density, as obtained by the two methods discussed in the text. The values obtained from the positions of the maxima of the probability distribution functions (blue dot) and from the average values (green square)are plotted as a function of temperature. Also shown is the best fit to data through T_c and ρ_c of the form $\rho \pm \rho_c = a|T - T_c| \pm b|T - T_c|^\beta$ with $a = 0.05$ and $b = 1.65$.

5.4   Conclusion

We end this chapter with a few comments. First, the major feature of our work is that we have determined in detail using finite-size scaling methods the phase diagram of a molecule with unusual architecture. We have chosen a very simple model for the interaction between these molecules; it would be straightforward to include other interactions in future work. We have shown that the model belongs to the Ising universality class as one might expect, since its order parameter is a scalar. It seems clear that future research will increasingly deal with unusual molecular architectures. We note in passing the fact that the molecule has a Y-shape has not resulted in an asymmetry of the type found for IgG on the high density side. There are several reasons for this. First, our model is two-dimensional. Second, we have
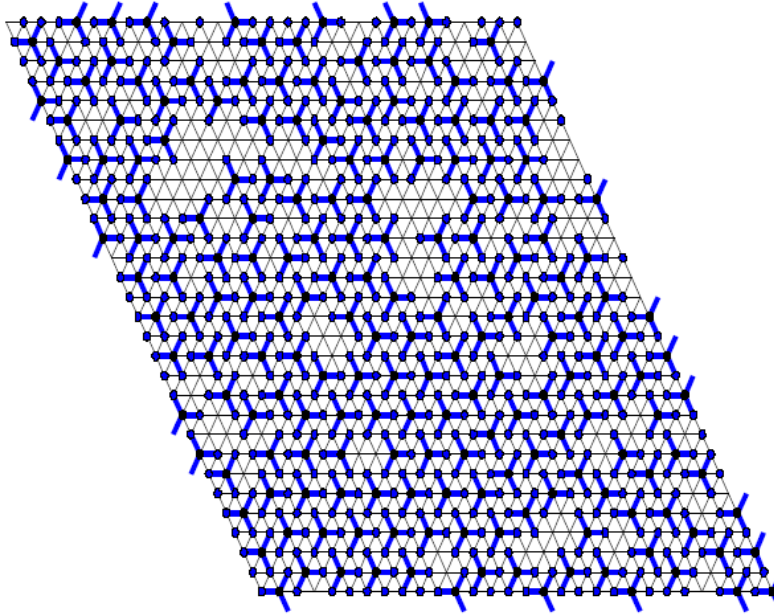
Figure 5.8: Sample of system size $L = 30$, at number density $\rho = 0.2156$ and temperature $T = 1.08$.

not taken into account in the model the large excluded volume effect that characterizes IgG, which Bendek *et al.* [133] have argued is responsible for its asymmetry. Indeed, the three-dimensional model of IgG studied by Li *et al.* [134] does have an excluded volume effect, and the phase diagram shows a pronounced asymmetry similar to that observed in experiment. It should also be noted that the reason our model has an asymmetry is due to the absence of a particle-hole symmetry, such as that present in the Ising model.

The first goal of future research is to apply patterned substrate binding similar to Rzysko and Borkowitz and determine how the critical temperature of the system is affected. This is to be completed in a future publication. Another direction for future research is to improve our model in order to describe the absorption of IgG on surfaces[134]. The inclusion of surfaces would require a somewhat more complex simulation algorithm, but would have the benefit of producing richer phase behavior. Another research direction would involve a more chemistry based, coarse-grained

model of IgG, such as the one proposed by Voth's group [135], to study not only its phase transitions, but its viscosity. Such models are especially useful in probing the electrostatic interaction between antibodies and its impact on ordering. Finally, we note that the rheological information (such as the viscosity) that could be obtained with a coarse-grained model is of considerable interest in the pharmaceutical world.

5.5 Acknowledgement

Chapter 6

Conclusion

The goal of the combined Janus ellipsoid projects was to determine the viability of Janus ellipsoids being implemented for encapsulation with controlled self-assembly. As noted in Chapter 1, some preliminary results pointed us in the direction of Janus ellipsoids with an aspect ratio of 0.6 and an interaction range of 0.2σ. Chapter 3 revolved around determining important characteristics of a system consisting solely of these short-range ellipsoids including cluster distributions, "micellization" temperature, and orientation correlation. As expected, the "micellization" temperature of this system was lower than that of the previously studied systems of interacting Janus spheres, with an interaction range of 0.5σ by Sciortino *et. al*[57].

The most interesting difference between our Janus ellipsoids and the aforementioned Janus spheres is the lack of micelles at low temperature and density. Below the micelle transition temperature in our system, it is not single-layer micelles that start forming, but bi-layer vesicles. We showed this through both the cluster distribution, as well as the orientation correlation of of the Janus ellipsoids, at temperatures below the transition temperature and low densities. The cluster distribution showed distinct peaks in the vesicle-sized cluster region and zero micelles. The orientation correlation function showed two peaks close to where the interacting particles are parallel or anti-parallel; This is a distinct characteristic of vesicle systems as compared to micelle forming systems, which have an orientation correlation function with a single peak, at which the interacting particles are nearly parallel.

Though our systems formed vesicles instead of micelles, we believe the phase diagram for our system would behave qualitatively like that of the Janus spheres studied by Sciortino *et. al*[56], based on B-2 scaling and physical arguments. They argued that the unique shape of the phase diagram found for Janus spheres is due to the formation of energetically stable micelles with the hard-core repulsive patches facing outward. While our system of Janus ellipsoids does not form micelles, it does form energetically stable clusters with hard-core repulsive patches facing outward, akin to the case of Janus spheres. Using a B_2 scaling approximation we estimated the phase diagram of our system based upon the phase diagram of the Janus spheres. Our approximate phase diagram had a the transition temperature close to that of the transition temperature we determined from the monomer density (ρ_1) versus density(ρ) plot.

After examining the system of Janus ellipsoids and determining that clusters of a narrow cluster size range is possible through self-assembly, in a separate study we considered a mixture of the Janus ellipsoids together with spheres that act as guest particles (e.g. drug particles), to explore the encapsulation efficiency of the Janus ellipsoid system. We explored varying the temperature, inter-particle interaction strength and range, and sphere size and found several trends. A characteristic that we noticed to be necessary for encapsulation was that the interaction between a sphere and an ellipsoid must be comparable to that between ellipsoids. Another characteristic is that the spheres can neither be too large nor too small compared to the size of the ellipsoids if they are to be encapsulated via self-assembly. One of the more important trends we noticed was that as the temperature increased, the ratio B_{es}/B_{ee} increased for all sphere radii and interaction strengths. This behavior suggests that annealing the system can be a viable method for increasing the efficiency of encapsulation since the bonding between ellipsoids and spheres is less effected than the bonding between ellipsoids.

Further work in encapsulation via Janus ellipsoids will most likely include a relatively similar parameter-space, except it will focus on prolate spheroids instead of oblate spheroids. Other work has shown that within a certain range of aspect ratio, prolate Janus spheroids form micelles with hard-core repulsive patches facing

outward, much like that of the Janus sphere. Apart from the aspect ratio, we would also consider an interaction between ellipsoids that is angularly dependent on the patch normal vectors.

Apart from Janus ellipsoids, we studied the adsorption of a model of Y-shaped molecules on a hexagonal lattice. We determined the two phase coexistence curve of our model through a series of Grand Canonical Monte Carlo simulations and found it to be rather symmetric (as a function of density) about the critical temperature. It is also very wide, and flat near the critical temperature. We also added a patterned substrate consisting of rows of sites with attractive binding site and found that as the strip width of these patterns increased, the critical temperature of the system decreased. The effect on critical temperature was also more apparent as the strength of the binding interaction was increased. This work is still in progress and its results will be added to the contents of chapter 5 and submitted for publication.

Future work in this adsorption project will include different patterns of substrate, different surface coverage of the patterns, as well as changing the interactions between arms of the Y-shaped molecule. The varying substrate patterns can be useful as a guide for other similarly patterned substrates, whereas changing the interaction between arms of the molecule can aid in determining the effect of anisotropy on the adsorption of these types of molecules.

Bibliography

[1] S. Ebbinghaus, A. Dhar, J. D. McDonald, and M. Gruebele, "Protein folding stability and dynamics imaged in a living cell," *Nature Methods*, vol. 7, pp. 7452–7458, 2014.

[2] S. Basak and K. Chattopadhyay, "Studies of protein folding and dynamics using single molecule fluorescence spectroscopy," *Phys. Chem. Chem. Phys.*, vol. 16, pp. 11139–11149, 2014.

[3] D. A. Edwards, F. Schneck, I. Zhang, A. M. J. Davis, H. Chen, and R. Langer, "Spontaneous vesicle formation at lipid bilayer membranes," *Biophysical Journal*, vol. 71, p. 1208, 1996.

[4] E. Kalb, S. Frey, and L. K. Tamm, "Formation of supported planar bilayers by fusion of vesicles to supported phospholipid monolayers," *Biochimica et Biophysica Acta (BBA) - Biomembranes*, vol. 1103, p. 307, 1992.

[5] K. Sugihara, B. Jang, M. Schneider, J. Voros, and T. Zambelli, "A universal method for planar lipid bilayer formation by freeze and thaw," *Soft Matter*, vol. 8, p. 5525, 2012.

[6] P. S. Cremer and S. G. Boxer, "Formation and spreading of lipid bilayers on planar glass supports," *J. Phys. Chem. B*, vol. 103, p. 2554, 1999.

[7] R. P. Richter, R. Berat, and A. R. Brisson, "Formation of solid-supported lipid bilayers: an integrated view," *Langmuir*, vol. 22, p. 3497, 2006.

[8] K. Y. Foo and B. H. Hameed, "Insights into the modeling of adsorption isotherm systems," *Chemical Engineering Journal*, vol. 156, p. 2, 2010.

[9] D. P. VanderWiel, M. Pruski, and T. S. King, "A kinetic study on the adsorption and reaction of hydrogen over silica-supported ruthenium and silver-ruthenium catalysts during the hydrogenation of carbon monoxide," *Journal of Catalysis*, vol. 188, p. 186, 1999.

[10] P. K. Schoch and J. Genzer, "Adsorption of "soft" spherical particles onto sinusoidally-corrugated substrates," *Soft Matter*, vol. 10, pp. 7452–7458, 2014.

[11] I. V. Malyar, D. A. Gorin, S. Santer, and S. V. Stetsyura, "Photocontrolled adsorption of polyelectrolyte molecules on a silicon substrate," *Langmuir*, vol. 29, no. 52, pp. 16058–16065, 2013.

[12] V. O. A. Pellegrini, N. Lei, M. Kyasaram, J. P. Olsen, S. F. Badino, M. S. Windahl, F. Colussi, N. Cruys-Bagger, K. Borch, and P. Westh, "Reversibility of substrate adsorption for the cellulases cel7a, cel6a, and cel7b from hypocrea jecorina," *Langmuir*, vol. 30, no. 42, pp. 12602–12609, 2014. PMID: 25322452.

[13] N. Dragneva, W. B. Floriano, D. Stauffer, R. C. Mawhinney, G. Fanchini, and O. Rubel, "Favorable adsorption of capped amino acids on graphene substrate driven by desolvation effect," *The Journal of Chemical Physics*, vol. 139, no. 17, pp. –, 2013.

[14] R. A. Griffiths, A. Williams, C. Oakland, J. Roberts, A. Vijayaraghavan, and T. Thomson, "Directed self-assembly of block copolymers for use in bit patterned media fabrication," *Journal of Physics D: Applied Physics*, vol. 46, no. 50, p. 503001, 2013.

[15] A. Tavakkoli K. G., K. W. Gotrik, A. F. Hannon, A. Alexander-Katz, C. A. Ross, and K. K. Berggren, "Templating three-dimensional self-assembled structures in bilayer block copolymer films," *Science*, vol. 336, no. 6086, pp. 1294–1298, 2012.

[16] E. R. Wright, R. A. McMillan, A. Cooper, R. P. Apkarian, and V. P. Conticello, "Thermoplastic elastomer hydrogels via self-assembly of an elastin-mimetic triblock polypeptide," *Adv. Funct. Mater.*, vol. 12, no. 149, p. 149, 2002.

[17] J. Liu, E. Sheina, T. Kowalewski, and R. D. McCullough, "Tuning the electrical conductivity and self-assembly of regioregular polythiophene by block copolymerization: Nanowire morphologies in new di- and triblock copolymers," *Angewandte Chemie International Edition*, vol. 41, no. 2, pp. 329–332, 2002.

[18] Y. Wang, M. Zhang, C. Moers, S. Chen, H. Xu, Z. Wang, X. Zhang, and Z. Li, "Block copolymer aggregates with photo-responsive switches: Towards a controllable supramolecular container," *Polymer*, vol. 50, no. 20, pp. 4821 – 4828, 2009.

[19] J.-F. Gohy and Y. Zhao, "Photo-responsive block copolymer micelles: design and behavior," *Chem. Soc. Rev.*, vol. 42, pp. 7117–7129, 2013.

[20] E. Winfree, F. Liu, L. A. Wenzler, and N. C. Seeman, "Design and self-assembly of two-dimensional dna crystals," *Nature*, vol. 394, p. 539, 1998.

[21] F. Liu, R. Sha, and N. C. Seeman, "Modifying the surface features of two-dimensional dna crystals," *J. Am. Chem. Soc.*, vol. 121, p. 917, 1999.

[22] J. Zheng, J. J. Birktoft, Y. Chen, T. Wang, R. Sha, P. E. Constantinou, S. L. Ginell, C. Mao, and N. C. Seeman, "From molecular to macroscopic via the rational design of a self-assembled 3d dna crystal," *Nature*, vol. 461, p. 74, 2009.

[23] W. M. Shih, J. D. Quispe, and G. F. Joyce, "A 1.7-kilobase single-stranded dna that folds into a nanoscale octahedron," *Nature*, vol. 427, p. 618, 2004.

[24] R. P. Goodman, I. A. T. Schaap, C. F. Tardin, C. M. Erben, R. M. Berry, C. F. Schmidt, and A. J. Turberfield, "Rapid chiral assembly of rigid dna bulding blocks for molecular nanofabrication," *Science*, vol. 310, p. 1661, 2005.

[25] Y. He, T. Ye, C. Zhang, A. E. Ribbe, W. Jiang, and C. Mao, "Hierarchical self-assembly of dna into symmetric supramolecular polyhedra," *Nature*, vol. 452, p. 198, 2008.

[26] O. Galkin, K. Chen, R. L. Nagel, R. E. Hirsch, and P. G. Vekilov, "Liquid-liquid separation in solutions of normal and sickle cell hemoglobin," *PNAS*, vol. 99, p. 8479, 2002.

[27] S. Kmoch, J. Brynda, B. Asfaw, K. Bezouska, P. Novak, P. Rexacova, L. Ondrova, M. Filipec, J. Sedlacek, and M. Elleder, "Link between anovel human γd-crystallin allele and a unique cataract phenotype explained by protein crystallography," *Human Molecular Genetics*, vol. 9, p. 1779, 2000.

[28] A. Pande, J. Pande, N. Asherie, A. Lomakin, O. Ogun, J. King, and G. B. Benedek, "Crystal cataracts: Human genetic cataract caused by protein crystallization," *PNAS*, vol. 98, p. 6116, 2001.

[29] D. M. Walsh, D. M. Hartley, Y. Kusumoto, Y. Fezoui, M. M. Condron, A. Lomakin, G. B. Benedek, D. J. Selkoe, and D. B. Teplow, "Amyloid β-protein fibrillogenesis: Structure and biological activity of protofibrillar intermediates," *Journal of Biological Chemistry*, vol. 274, p. 25945, 1999.

[30] C. P. Brangwynne, C. R. Eckmann, D. S. Courson, A. Rybarska, C. Hoege, J. Gharakhani, F. Julicher, and A. A. Hyman, "Germline p granules are liquid droplets that localize by controlled dissolution/condensation," *Science*, vol. 324, p. 1729, 2009.

[31] M. Maldovan and E. L. Thomas, "Diamond-structured photonic crystals," *Nature Materials*, vol. 3, p. 593, 2004.

[32] S. C. Glotzer and M. J. Solomon, "Anisotropy of building blocks and their assembly into complex structures," *Nature Materials*, vol. 6, p. 557, 2007.

[33] S. Pradhan, L. Xu, and S. Chen, "Janus nanoparticles by interfacial engineering," *Advanced Functional Materials*, vol. 17, no. 14, pp. 2385–2392, 2007.

[34] L. Hong, A. Cacciuto, E. Luijten, and S. Granick, "Clusters of amphiphilic colloidal spheres," *Langmuir*, vol. 24, no. 3, pp. 621–625, 2008. PMID: 18181655.

[35] L. Hong, A. Cacciuto, E. Luijten, and S. Granick, "Clusters of charged janus spheres," *Nano Letters*, vol. 6, no. 11, p. 2510, 2006.

[36] C. Peng, I. Lazo, S. V. Shiyanovskii, and O. D. Lavrentovich, "Induced-charge electro-osmosis around metal and janus spheres in water: Patterns of flow and breaking symmetries," *Phys. Rev. E*, vol. 90, p. 051002, Nov 2014.

[37] F. Sciortino, A. Giacometti, and G. Pastore, "Phase diagram of janus particles," *Phys. Rev. Lett.*, vol. 103, p. 237801, Nov 2009.

[38] A. Giacometti, C. Ggelein, F. Lado, F. Sciortino, S. Ferrari, and G. Pastore, "From square-well to janus: Improved algorithm for integral equation theory and comparison with thermodynamic perturbation theory within the kern-frenkel model," *The Journal of Chemical Physics*, vol. 140, no. 9, pp. –, 2014.

[39] F. Sciortino, A. Giacometti, and G. Pastore, "A numerical study of one-patch colloidal particles: from square-well to janus," *Phys. Chem. Chem. Phys.*, vol. 12, pp. 11869–11877, 2010.

[40] T. Vissers, Z. Preisler, F. Smallenburg, M. Dijkstra, and F. Sciortino, "Predicting crystals of janus colloids," *The Journal of Chemical Physics*, vol. 138, no. 16, pp. –, 2013.

[41] Y. Liu, W. Li, T. Perez, J. D. Gunton, and G. Brett, "Self assembly of janus ellipsoids," *Langmuir*, vol. 28, no. 1, pp. 3–9, 2012. PMID: 22171980.

[42] A. A. Shah, B. Schultz, W. Zhang, S. C. Glotzer, and M. J. Solomon, "Actuation of shape-memory colloidal fibres of janus ellipsoids," *Nature Mat.*, vol. 14, p. 17, 2015.

[43] X.-C. Luu, J. Yu, and A. Striolo, "Ellipsoidal janus nanoparticles adsorbed at the wateroil interface: Some evidence of emergent behavior," *The Journal of Physical Chemistry B*, vol. 117, no. 44, pp. 13922–13929, 2013. PMID: 24087908.

[44] X.-C. Luu and A. Striolo, "Ellipsoidal janus nanoparticles assembled at spherical oil/water interfaces," *The Journal of Physical Chemistry B*, vol. 118, no. 47, pp. 13737–13743, 2014. PMID: 25358124.

[45] B. M. Mattix, T. R. Olsen, M. Casco, L. Reese, J. T. Poole, J. Zhang, R. P. Visconti, A. Simionescu, D. T. Simionescu, and F. Alexis, "Janus magnetic cellular spheroids for vascular tissue engineering," *Biomaterials*, vol. 35, no. 3, pp. 949 – 960, 2014.

[46] N. L. de Macedo, F. da Silva Matuda, L. G. S. de Macedo, M. B. Gonzalez, S. M. Ouchi, and Y. R. Carvalho, "Bone defect regeneration with bioactive glass implantation in rats," *Journal of Applied Oral Science*, vol. 12, no. 2, p. 137, 2004.

[47] F. Zhang, E. Kang, K. Neoh, P. Wang, and K. Tan, "Surface modification of stainless steel by grafting of poly(ethylene glycol) for reduction in protein adsorption," *Biomaterials*, vol. 22, no. 12, pp. 1541 – 1548, 2001.

[48] F. Shayeganfar and A. Rochefort, "Electronic properties of self-assembled trimesic acid monolayer on graphene," *Langmuir*, vol. 30, no. 32, pp. 9707–9716, 2014. PMID: 25072917.

[49] A. B. Pawar and I. Kretzschmar, "Multifunctional patchy particles by glancing angle deposition," *Langmuir*, vol. 25, p. 9057, 2009.

[50] V. N. Manoharan, M.T.Elsesser, and D.J.Pine, "Dense packing and symmetry in small clusters of microspheres," *Science*, vol. 301, p. 483, 2003.

[51] S. Jiang, Q. Chen, M. Tripathy, E. Luijten, K. S. Schweizer, and S. Granick, "Janus particle synthesis and assembly," *Adv. Mater.*, vol. 22, p. 1060, 2010.

[52] Q. Chen, J. K.Whitmer, S. Jiang, S. C. Bae, E. Luijten, and S. Granick, "Supracolloidal reaction kinetics of janus spheres," *Science*, vol. 331, p. 199, 2011.

[53] Q. Chen, S. C. Bae, and S. Granick, "Directed self-assembly of a colloidal kagome lattice," *Nature*, vol. 469, p. 381, 2011.

[54] S. C. Glotzer and M. J. Solomon, "Anisotropy of building blocks and their assembly into complex structures," *Nature Materials*, vol. 6, p. 557, 2007.

[55] J. D. Gunton, A. Shiryayev, and D. Pagan, *Protein Condensation: Kinetic Pathways to Crystallization and Disease*. Cambridge University Press: Cambridge, 2007.

[56] F. Sciortino, A. Giacometti, and G. Pastore, "Phase diagram of janus particles," *Phys. Rev. Lett.*, vol. 103, p. 237801, 2009.

[57] F. Sciortino, A. Giacometti, and G. Pastore, "A numerical study of one-patch colloidal particles: from square-well to janus," *Phys. Chem. Chem. Phys.*, vol. 12, p. 11869, 2010.

[58] G. Krylova, L. Giovanetti, F. G. Requejo, N. M. Dimitrijevic, A. Prakpenka, and E. V. Shevchenko, "Study of nucleation and growth mechanism of the metallic nanodumbells," *J. Am. Chem. Soc.*, vol. 134, p. 4384, 2012.

[59] J. He, M. Perez, P. Zhang, Y. Liu, T. Babu, J. Gong, and Z. Nie, "A general approach to synthesize asymmetric hybrid nanoparticles by interfacial reactions," *J. Am. Chem. Soc.*, vol. 134, p. 3639, 2012.

[60] Y. Gao and Y. Yu, "How half-coated janus particles enter cells," *J. Am. Chem. Soc.*, vol. 135, p. 19091, 2013.

[61] K. H. Roh, D. C. Martin, and J. Lahann, "Biphasic janus particles with nanoscale anisotropy," *Nat. Mater.*, vol. 4, p. 759, 2005.

[62] S. H. Kim, S. J. Jeon, W. C. Jeong, H. S. Park, and S. M. Yang, "Optofluidic synthesis of electroresponsive photonic janus balls with isotropic structural colors," *Adv. Mater.*, vol. 20, p. 4129, 2008.

[63] A. Reinhardt, A. J. Williamson, J. P. K. Doye, J. Carrete, L. M. Varela, and A. A. Louis, "Re-entrant phase behavior for systems with competition between phaseseparation and self-assembly," *J. Chem. Phys.*, vol. 134, p. 104905, 2011.

[64] L. Hong, A. Cacciuto, E. Luitjen, and S. Granick, "Clusters of charged janus spheres," *Nano Lett.*, vol. 6, p. 2510, 2006.

[65] N. Kern and D. Frenkel, "Fluid-fluid coexistence in colloidal systems with short-ranged strongly directional attraction," *J. Chem. Phys.*, vol. 118, p. 9882, 2003.

[66] T. Vissers, Z. Preisler, F. Smallenburg, M. Dijkstra, and F. Sciortino, "Predicting crystals of janus colloids," *J. Chem. Phys*, vol. 138, p. 164505, 2013.

[67] R. D. Stanimirova, T. D. Gurkov, P. A. Kraichevsky, K. T. Balashev, S. D. Stoyanov, and E. G. Pelan, "Surface pressure and elasticity of hydrophobin hfbii layers on the air-water interface: Rheology versus structure detected by afm imaging," *Langmuir*, vol. 29, p. 6053, 2013.

[68] K. Simons, A. Helenuis, K. Leonard, M. Sarvas, and M. J. Gething, "M. j. formation of protein micelles from amphiphilic membrane proteins," *Proc. Natl. Acad. Sci. USA*, vol. 75, p. 5306, 1978.

[69] Y. Liu, W. Li, T. Perez, J. D. Gunton, and G. Brett, "Self-assembly of janus ellipsoids," *Langmuir*, vol. 28, p. 3, 2012.

[70] W. Li and J. D. Gunton, "Self-assembly of janus ellipsoids ii: Janus prolate spheroids," *Langmuir*, vol. 29, p. 8517, 2013.

[71] B. J. Berne and P. Pechukas, "Gaussian model potentials for molecular interactions," *J. Chem. Phys.*, vol. 56, p. 4213, 1971.

[72] A. Bhattacharyay and A. Toisi, "Self-assembly of sparsely distributed molecules: An efficient cluster algorithm," *Chem. Phys. Lett.*, vol. 458, p. 210, 2008.

[73] R. H. Swendsen and J. S. Wang, "Nonuniversal critical dynamics in monte carlo simulations," *Phys. Rev. Lett.*, vol. 58, p. 86, 1987.

[74] B. L. Neal, D. Asthagiri, O. D. Velev, A. M. Lenhoff, and E. W. Kaler, "Why is the osmotic second virial coefficient related to protein crystallization," *J. Cryst. Growth*, vol. 196, p. 377, 1999.

[75] J. A. Cuesta and C. F. Tejero, "Second virial coefficient of the d-dimensional hard gaussian overlap model," *Phys. Lett. A*, vol. 152, p. 15, 1991.

[76] M. G. Noro and D. Frenkel, "Extended corresponding states behavior for particles with variable range interactions," *J. Chem. Phys.*, vol. 113, p. 2941, 2000.

[77] G. Foffi and F. Sciortino, "On the possibility of extending the noro-frenkel generalized law of correspondent states to nonisotropic patchy interactions," *J. Phys. Chem. B*, vol. 111, p. 9702, 2007.

[78] W. Li, Y. Liu, G. Brett, and J. D. Gunton, "Encapsulation by janus spheroids," *Soft Matter*, vol. 8, p. 6027, 2012.

[79] E. Mathiowitz, J. S. Jacob, Y. S. Jong, G. P. Carino, D. E. Chickering, P. Chaturvedi, C. A. Santos, K. Vijayaraghavan, S. Montgomery, M. Bassett, and C. Morrel, "Biologically erodable microspheres as potential oral drug delivery systems," *Nature*, vol. 386, p. 410, 1997.

[80] D. Sutton, N. Nasongkla, E. Blanco, and J. Gao, "Functionalized micellar systems for cancer targeted drug delivery," *Pharmaceut. Res.*, vol. 24, p. 1029, 2007.

[81] S. Cohen, T. Yoshioka, M. Lucarelli, L. Hwang, and R. Langer, "Controlled delivery systems for proteins based on poly(lactic/glycolic acid) microspheres," *Pharmaceut. Res.*, vol. 8, p. 713, 1991.

[82] C. S. Peyratout and L. Dähne, "Tailor-Made Polyelectrolyte Microcapsules: From Multilayers to Smart Containers," *Angew. Chem. Int. Ed.*, vol. 43, pp. 3762–3783, 2004.

[83] R. Ciriminna, M. Sciortino, G. Alonzo, A. de Schrijver, and M. Pagliaro, "From Molecules to Systems: Sol-Gel Microencapsulation in Silica-Based Materials," *Chem. Rev.*, vol. 111, pp. 765–789, 2011.

[84] S. Gouin, "Microencapsulation: industrial appraisal of existing technologies and trends," *Trends Food Sci. Technol.*, vol. 15, pp. 330–347, 2004.

[85] T. M. Allen and P. R. Cullis, "Drug Delivery Systems: Entering the Mainstream," *Science*, vol. 303, pp. 1818–1822, 2004.

[86] M. M. Caruso, D. A. Delafuente, V. Ho, N. R. Sottos, J. S. Moore, and S. R. White, "Solvent-Promoted Self-Healing Epoxy Materials," *Macromolecules*, vol. 40, pp. 8830–8832, 2007.

[87] S. H. Cho, S. R. White, and P. V. Braun, "Self-Healing Polymer Coatings," *Advanced Materials*, vol. 21, pp. 645–649, 2009.

[88] R. M. Crooks, M. Zhao, L. Sun, V. Chechik, and L. K. Yeung, "Dendrimer-Encapsulated Metal Nanoparticles: Synthesis, Characterization, and Applications to Catalysis," *Acc. Chem. Res.*, vol. 34, pp. 181–190, 2001.

[89] A. K. Anal and H. Singh, "Recent advances in microencapsulation of probiotics for industrial applications and targeted delivery," *Trends Food Sci. Technol.*, vol. 18, pp. 240–251, 2007.

[90] M. A. Augustin and Y. Hemar, "Nano- and micro-structured assemblies for encapsulation of food ingredients," *Chem. Soc. Rev.*, vol. 38, pp. 902–912, 2009.

[91] R. Haag, "Supramolecular Drug-Delivery Systems Based on Polymeric Core-Shell Architectures," *Angew. Chem. Int. Ed.*, vol. 43, pp. 278–282, 2004.

[92] L. Zhang, J. M. Chan, F. X. Gu, J.-W. Rhee, A. Z. Wang, A. F. Radovic-Moreno, F. Alexis, R. Langer, and O. C. Farokhzad, "Self-Assembled Lipid-Polymer Hybrid Nanoparticles: A Robust Drug Delivery Platform," *ACS Nano*, vol. 2, pp. 1696–1702, 2008.

[93] A. K. Patri, J. F. Kukowska-Latallo, and J. R. Baker Jr., "Targeted drug delivery with dendrimers: Comparison of the release kinetics of covalently conjugated drug and non-covalent drug inclusion complex," *Advanced Drug Delivery Reviews*, vol. 57, pp. 2203–2214, 2005.

[94] H. Chen, R. C. MacDonald, S. Li, N. L. Krett, S. T. Rosen, and T. V. O'Halloran, "Lipid Encapsulation of Arsenic Trioxide Attenuates Cytotoxicity and Allows for Controlled Anticancer Drug Release," *J. Am. Chem. Soc.*, vol. 128, pp. 13348–13349, 2006.

[95] A. Rösler, G. W. Vandermeulen, and H.-A. Klok, "Advanced drug delivery devices via self-assembly of amphiphilic block copolymers," *Advanced Drug Delivery Reviews*, vol. 64, pp. 270–279, 2012.

[96] Y.-G. Kim, S.-K. Oh, and R. M. Crooks, "Preparation and Characterization of 1-2 nm Dendrimer-Encapsulated Gold Nanoparticles Having Very Narrow Size Distributions," *Chem. Mater.*, vol. 16, pp. 167–172, 2004.

[97] L. M. Dominak and C. D. Keating, "Polymer Encapsulation within Giant Lipid Vesicles," *Langmuir*, vol. 23, pp. 7148–7154, 2007.

[98] I. G. Loscertales, A. Barrero, I. Guerrero, R. Cortijo, M. Marquez, and A. M. Gañán-Calvo, "Micro/Nano Encapsulation via Electrified Coaxial Liquid Jets," *Science*, vol. 295, pp. 1695–1698, 2002.

[99] M.-W. Chang, E. Stride, and M. Edirisinghe, "A novel process for drug encapsulation using a liquid to vapour phase change material ," *Soft Matter*, vol. 5, pp. 5029–5036, 2009.

[100] J. Du and R. K. O'Reilly, "Advances and challenges in smart and functional polymer vesicles," *Soft Matter*, vol. 5, pp. 3544–3561, 2009.

[101] S. Jiang, Q. Chen, M. Tripathy, E. Luijten, K. S. Schweizer, and S. Granick, "Janus Particle Synthesis and Assembly," *Advanced Materials*, vol. 22, pp. 1060–1071, 2010.

[102] J. Du and R. K. O'Reilly, "Anisotropic particles with patchy, multicompartment and Janus architectures: preparation and application," *Chem. Soc. Rev.*, vol. 40, p. 2402, 2011.

[103] A. Walther and A. H. E. Müller, "Janus Particles: Synthesis, Self-Assembly, Physical Properties, and Applications," *Chem. Rev.*, vol. 113, pp. 5194–5261, 2013.

[104] Q. Chen, J. K.Whitmer, S. Jiang, S. C. Bae, E. Luijten, and S. Granick, "Supracolloidal Reaction Kinetics of Janus Spheres," *Science*, vol. 331, p. 199, 2011.

[105] F. Sciortino, A. Giacometti, and G. Pastore, "Phase Diagram of Janus Particles," *Physical Review Letters*, vol. 103, p. 237801, 2009.

[106] F. Sciortino, A. Giacometti, and G. Pastore, "A numerical study of one-patch colloidal particles: from square-well to Janus," *Phys. Chem. Chem. Phys.*, vol. 12, p. 11869, 2010.

[107] R. Fantoni, A. Giacometti, F. Sciortinoc, and G. Pastore, "Cluster theory of Janus particles," *Soft Matter*, vol. 7, p. 2419, 2011.

[108] G. Rosenthal, K. E. Gubbins, and S. H. L. Klapp, "Self-assembly of model amphiphilic Janus particles," *J. Chem. Phys.*, vol. 136, p. 174901, 2012.

[109] Y. Liu, W. Li, T. Perez, J. D. Gunton, and G. Brett, "Self Assembly of Janus Ellipsoids," *Langmuir*, vol. 28, p. 3, 2012.

[110] Z.-W. Li, Z.-Y. Lu, Z.-Y. Sun, and L.-J. An, "Model, self-assembly structures, and phase diagram of soft Janus particles," *Soft Matter*, vol. 8, p. 6693, 2012.

[111] W. Li and J. D. Gunton, "Self-Assembly of Janus Ellipsoids II: Janus Prolate Spheroids," *Langmuir*, vol. 29, pp. 8517–8523, 2013.

[112] D. Ruth, J. D. Gunton, J. M. Rickman, and W. Li, "The Impact of Anisotropy and Interaction Range on the Self-Assembly of Janus Ellipsoids," *J. Chem. Phys.*, vol. 141, p. 214903, 2014.

[113] W. Li, Y. Liu, G. Brett, and J. D. Gunton, "Encapsulation by Janus spheroids," *Soft Matter*, vol. 8, p. 6027, 2012.

[114] M. Vallet-Regí, F. Balas, and D. Arcos, "Mesoporous Materials for Drug Delivery," *Angew. Chem. Int. Ed.*, vol. 46, pp. 7548–7558, 2007.

[115] B. J. Berne and P. Pechukas, "Gaussian Model Potentials for Molecular Interactions," *J. Chem. Phys.*, vol. 56, p. 4213, 1972.

[116] A. W. Wilber, J. P. K. Doye, and A. A. Louis, "Self-assembly of monodisperse clusters: Dependence on target geometry," *J. Chem. Phys.*, vol. 131, p. 175101, 2009.

[117] D. W. Sinkovits, S. A. Barr, and E. Luijten, "Rejection-free Monte Carlo scheme for anisotropic particles," *J. Chem. Phys.*, vol. 136, p. 144111, 2012.

[118] L. Vega, E. de Miguel, L. F. Rull, G. Jackson, and I. A. McLure, "Phase equilibria and critical behavior of square-well fluids of variable width by Gibbs ensemble Monte Carlo simulation," *J. Chem. Phys.*, vol. 96, p. 2296, 1992.

[119] N. Kern and D. Frenkel, "Fluid-fluid coexistence in colloidal systems with short-ranged strongly directional attraction," *J. Chem. Phys.*, vol. 118, p. 9882, 2003.

[120] S. Rentsch, R. Pericet-Camara, G. Papastavrou, and M. Borkovec, "Probing the validity of the Derjaguin approximation for heterogeneous colloidal particles," *Phys. Chem. Chem. Phys.*, vol. 8, pp. 2531–2538, 2006.

[121] R. Aveyard, "Can Janus particles give thermodynamically stable Pickering emulsions?," *Soft Matter*, vol. 8, pp. 5233–5240, 2012.

[122] T. M. Ruhland, A. H. Gröschel, N. Ballard, T. S. Skelhon, A. Walther, A. H. E. Müller, and S. A. F. Bon, "Influence of Janus Particle Shape on Their Interfacial Behavior at Liquid-Liquid Interfaces," *Langmuir*, vol. 29, pp. 1388–1394, 2013.

[123] J. G. Gay and B. J. Berne, "Modification of the overlap potential to mimic a linear site-site potential," *J. Chem. Phys.*, vol. 74, p. 3316, 1981.

[124] P. Szabelski, W. Rzysko, T. Pancyzk, E. Ghijsens, K. Tahara, Y. Tobe, and S. D. Feyter, "Self-assembly of molecular tripods in two dimensions: structure and thermodynamics from computer simulations," *RSC Adv.*, vol. 3, p. 25159, 2013.

[125] W. Rzysko and M. Borowko, "Monte carlo study of adsorption of heteronuclear dimers on heterogeneous surfaces," *Thin Solid Films*, vol. 425, p. 304, 2003.

[126] A. D. Bruce and N. B. Wilding, "Scaling fields and universality of the liquid-gas critical point," *Phys. Rev. Lett.*, vol. 68, p. 193, 1992.

[127] N. B. Wilding and A. D. Bruce, "Density fluctuations and field mixing in the critical fluid," *J. Phys. Condens. Matter*, vol. 4, p. 3087, 1992.

[128] R. Toral and P. Colet, *Stochastic Numerical Methods*. Wiley-VCH, 2014.

[129] N. B. Wilding, "Critical-point and coexistence-curve properties of the lennard-jones fluid: A finite-size scaling study," *Phys. Rev. E*, vol. 52, p. 602, 1995.

[130] X. Li, S. Lettieri, N. Wentzel, and J. D. Gunton, "Phase diagram of a model of nanoparticles in electrolyte solutions," *J. Chem. Phys.*, vol. 129, p. 164113, 2008.

[131] M. Barma and M. E. Fisher, "Two-dimensional ising-like systems: Corrections to scaling in the klauder and double-gaussian models," *Phys. Rev. B*, vol. 31, p. 5954, 1985.

[132] B. Nienhuis, "Analytical calculation of two leading exponents of the dilute potts model," *J. Phys. A: Math. Gen.*, vol. 15, p. 199, 1982.

[133] Y. Wang, A. Lomakin, R. F. Latypov, J. P. Laubach, T. Hideshima, P. G. Richardson, N. C. Munshi, K. C. Anderson, and G. B. Bennedek, "Phase transitions in human igg solutions," *J. Chem. Phys*, vol. 139, p. 121904, 2013.

[134] J. Li, R. Rajagopalan, and J. Jiang, "Polymer-induced phase separation and crystallization in immunoglobulin g solutions," *J. Chem. Phys.*, vol. 128, p. 205105, 2008.

[135] A. Chaudri, I. E. Zarraga, S. Yadav, T. W. Patapoff, S. J. Shire, and G. A. Voth, "Analytical calculation of two leading exponents of the dilute potts modelthe role of amino acid sequence in the self-association of therapeutic monoclonal antibodies: Insights from coarse-grained modeling," *J. of Phys. Chem. B*, vol. 117, p. 1269, 2012.

Vita

Donovan Paul Ruth was raised in a rural part of the Lehigh Valley in Pennsylvania. He attended Northwestern Lehigh High school and graduated in 2006 then entered Kutztown University of Pennsylvania where he received his Bachelor of Science in Physics. In August 2010 he started graduate studies at Lehigh University and earned a PhD. in Physics in May 2015.